Exciton Dynamics in Coupled Nano-Rings of Dipolar Quantum Emitters

Masterarbeit
zur Erlangung des akademischen Grades
Master of Science

eingereicht an der
Fakultät für Mathematik, Informatik und Physik
der Leopold-Franzens-Universität Innsbruck

von
Verena Scheil, BSc

Innsbruck, den 22.02.2022

Betreuer:
Univ.-Prof. Dr. Helmut Ritsch
Mitwirkende Betreuer:
Raphael Holzinger, MSc.
Maria Moreno-Cardoner, PhD.
Institut für Theoretische Physik

Abstract

We study the collective radiative dynamics of special nanoscopic arrays of point-like dipole emitters. A single ring of sub-wavelength spaced dipole-coupled quantum emitters possesses only very few radiant but many extraordinarily subradiant collective modes. These exhibit a 3D-confined spatial radiation field pattern forming a nano-scale high-Q optical resonator. Motivated by structures commonly appearing in natural light harvesting structures we extend these studies to concentric double rings. Proven to produce promising results in the single-ring case, a generalized spin-wave Ansatz was chosen to investigate the radiation properties of double-ring structures. From symmetry considerations one can conclude that the excitonic wave functions are composed of spin-waves with equal or opposite phase, allowing us to analytically study the rich behaviour of the super- and subradiant properties of these eigenmodes. Subsequently we proceed to analyze such collective eigenmodes in structures mimicking the light-harvesting complexes in purple photosynthetic bacteria and highlight the special properties for nature's particular choice of angles.

Zusammenfassung

Wir untersuchen die kollektive Strahlungsdynamik spezieller nanoskopischer Anordnungen punktförmiger Dipolemitter. Ein einzelner Ring von dipolgekoppelten Quantenemittern mit Subwellenlängenabstand besitzt nur sehr wenige radiante, aber viele außerordentlich subradiante kollektive Moden. Diese weisen ein 3D-begrenztes, räumliches Strahlungsfeldmuster auf, das einen optischen High-Q-Resonator im Nanomaßstab bildet. Motiviert durch Strukturen, die üblicherweise in natürlichen Lichtsammelkomplexen auftreten, erweitern wir diese Studien auf konzentrische Doppelringe. Da sich im Einzelringfall nachweislich vielversprechende Ergebnisse ergeben, wurde ein verallgemeinerter Spinwellenansatz gewählt, um die Strahlungseigenschaften von Doppelringstrukturen zu untersuchen. Aus Symmetrieüberlegungen kann man schlussfolgern, dass die exzitonischen Wellenfunktionen aus Spinwellen mit gleicher oder entgegengesetzter Phase bestehen, was es uns ermöglicht, das reiche Verhalten der super- und subradianten Eigenschaften dieser Eigenmoden analytisch zu untersuchen. Anschließend analysieren wir solche kollektiven Eigenmoden in Strukturen, die die Lichtsammelkomplexe in violetten photosynthetischen Bakterien nachahmen, und heben die besonderen Eigenschaften für die natürliche Wahl der Winkel hervor.

Danksagung

Ganz besonders danken möchte ich an dieser Stelle meinen Eltern, die mir mein Studium überhaupt erst ermöglicht und mich immer und überall, sowohl während des Studiums, als auch außerhalb der Uni, unterstützt haben. Natürlich gilt der Dank auch meiner wunderbaren Schwester und dem Rest meiner Familie, auf die ich mich immer verlassen kann und die mir mit Rat und Tat zur Seite stehen.
Bedanken möchte ich mich auch bei den Mitgliedern dieser Arbeitsgruppe, die mich sehr freundlich aufgenommen haben und mir bei Fragen immer behilflich waren. Ganz besonders möchte ich mich hier bei Maria Moreno-Cardoner und Raphael Holzinger bedanken, die mir sehr geholfen und mich mit hilfreichen Tipps und Diskussionen unterstützt haben. Spezieller Dank gilt an dieser Stelle meinem Betreuer, Prof. Helmut Ritsch, ohne den diese Arbeit nicht entstanden wäre, der sie mit immer neuen Ideen und Ansätzen bereichert hat und mich immer für dieses interessante Projekt begeistern konnte.
Zuallerletzt bedanke ich mich bei meinen tollen Freunden, mit denen ich diese aufregende Zeit verbringen durfte. Ganz besonders bedanke ich mich hier bei Fabiola, Mara, Francesco, Lorenz, Julian, Regina und Adrian und den, nicht explizit genannten, übrigen Nablas, die mich von dem Unialltag abgelenkt und mir den ein oder anderen Tag versüßt haben. Ihr seid alle ganz herrlich. Außerdem ein dickes Dankeschön an Sarah, Amal und Nefeli und an meinen Bürokumpanen Fabi für die schönen Mittags- und Kaffeepausen. Auch meinen übrigen Studienkollegen möchte ich hier für die gemeinsame Zeit danken.

Ein ganz, ganz großes Dankeschön an alle Genannten und ausversehen Nicht-Genannten.

Contents

Chapter 1

Introduction

The earth continuously receives about 120.000 TW solar energy [1], which exceeds the annual worldwide energy consumption rate by 15.000 times [2]. It comes along that in contrast to other energy sources, solar energy is - at least for the lifetime of the sun - completely renewable. Photosynthesis as an energy transfer mechanism plays a crucial role for living organisms and evolution has created optimal processes of converting solar to chemical energy within photosynthetic systems [3]. An essential step in the photosynthetic process is to harvest sunlight and to transport it via light-harvesting complexes towards the reaction center, where the actual conversion of energy takes place [4]. Recent theoretical and experimental studies seem to indicate that quantum coherence plays a crucial role in these processes [5]. Understanding them in detail is thus of prime importance in order to harness the enormous amount of solar energy by developing more efficient photovoltaic devices or artificial photosynthesis [2]. However, an efficient and in particular a controllable energy transfer is not only essential in photosynthetic processes but has a wide variety of application as in quantum communication or near-field communication protocols [6].

A factor limiting the control on the energy transfer is spontaneous emission of photons arising from vacuum fluctuations of the electromagnetic field – a non-desirable process in most experiments. As shown in [6], keeping the spontaneous emission rate low and preparing atoms in long-lived, subradiant states, aids the process of excitation transport between two independent chains of regularly arranged quantum emitters. Collective effects in a system of subwavelength-spaced identical quantum emitters can either enhance or suppress spontaneous emission, as already predicted by Dicke [7]. In case of enhancement, i.e., constructive interference of the radiation of different atoms, one talks about the so-called superradiance that decreases the lifetime of the collective mode. As Dicke predicted, a dense ensemble of quantum emitters in a symmetric superposition can show superradiance. In contrast to that, suppression of the decay, i.e., subradiance, in an infinite 1D chain of subwavelength-spaced atoms occurs, if the magnitude of the wave vector of the collective exciton is higher than the free-space photon wave vector [8]. In this case, the optical modes are guided by the array, and are decoupled from free space radiation leading to perfectly dark excitons. For a finite chain, the photon can only scatter off the ends of the chain, and it was found that the lifetime of a collective state grows with the third power of the number of chain atoms [9]. This has also been proven experimentally with an ensemble of gold nano-particles [10]. The special properties of sub- and superradiant states have been subject of research in several different works, as for example in [11]. Here, as it's standing to reason, the chain of atoms was closed to a circle of quantum emitters in order to circumvent the energy loss at the end of the

chain and hence decrease the decay rate even further. It was found that the subradiant decay rate decreases exponentially with the number of atoms in the system.

As mentioned before, quantum coherence seems to be relevant in the energy transfer in some photosynthetic complexes such as in purple bacterium Rhodopseudomonas acidophila [12]. This bacterium developed specialized antenna units, namely light-harvesting I (LH-I) and light-harvesting II (LH-II) complexes that harvest sunlight and transfer this energy within and between the complexes, respectively, towards the reaction center [4], as it is schematically depicted in Fig. 1.1. These nine-fold light-harvesting complexes have a simple structure. From X-ray crystallography data, it was found that they are made up of three rings, each consisting of 9 pigments [4]. In particular, the major pigments are bacteriochlorophyll (BChl). In LH-II complexes, one third of the BChls form the so-called B800 ring, i.e., the 800 nm wavelength energy band. The other BChls build the B850 band. When interacting with visible light, these pigments can be modeled as a two-level system with an optical dipole transition. Given the size of these complexes and distances between the pigments (on the order of $d/\lambda \sim 1/100$) we then expect dipole-dipole interactions to be relevant enough to lead to strong cooperative phenomena that can modify the dynamics of the energy transfer. Using this simplistic structure, an intriguing question is, whether nature chooses this particular configuration - the specific choice of distances between the rings and atoms or the dipole orientations - on purpose, aiming for a minimization of the loss of energy in the system and providing an efficient energy transport [6].

Here, we want to study the B850 energy band and its configuration under the aspect of subradiance. Ultimately, we want to obtain information about nature's particular choice of angles and distances in the system. To do this, we need to extend the results presented in [11] where a system of two neighbouring rings is studied, to the case of two rings, where one ring possesses an additional z component perpendicular to the plane of the lower ring in its position vector. Furthermore we want to find an analytical way of studying the exciton dynamics in that case.

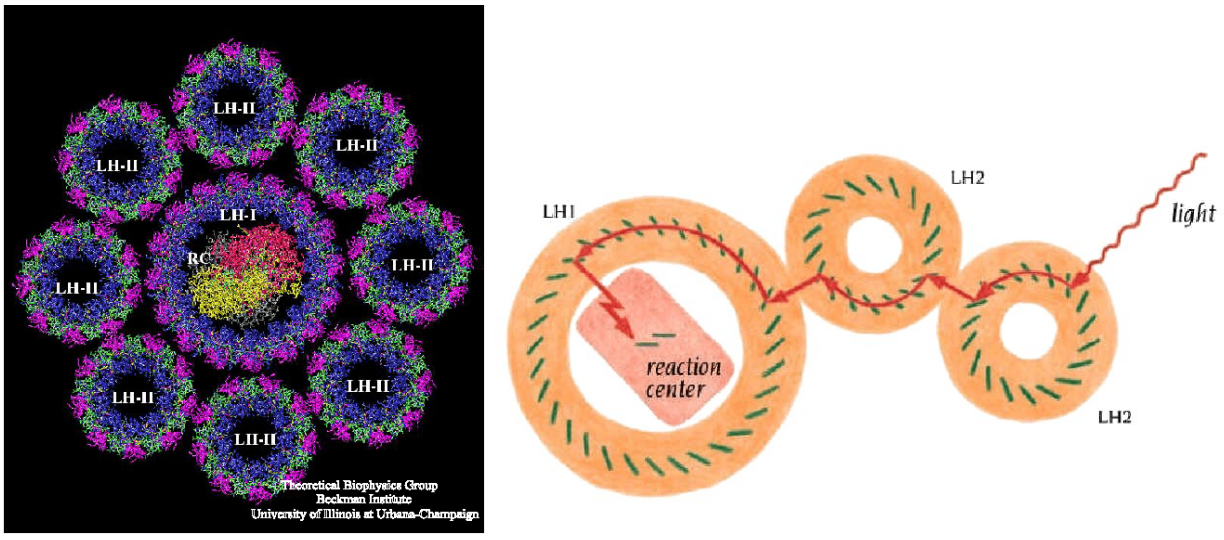

(a) (b)

Figure 1.1: *Schematic pictures of* **(a)** *light-harvesting complexes and* **(b)** *light-capturing pathway in purple bacteria towards the reaction center, extracted from [13] and [14], respectively.*

Chapter 2

Fundamental Concepts and Models

In this chapter we discuss the underlying concepts all subsequent studies are based on. In essence we study the interaction of a light field with a collection of dense atoms including inter-atomic coupling via dipole-dipole interaction. As photons can enter and leave the interaction volume we need to model this as an open quantum system. Therefore we first find a corresponding Quantum Langevin equation and secondly we construct a Master equation. Both give rise to the whole system dynamics, however, depending on the particular case, one of them is easier to solve. The dynamics include a special phenomenon, i.e., sub- and superradiance, that we discuss using the trivial example of two coupled quantum emitters.

2.1 Quantum Mechanics of Electric Dipole Transitions

The interaction within a sub-wavelength spaced collection of identical two-level quantum emitters with transition frequency ω_0 is led back to the coupling of the dipole transition of each emitter with a radiation field. In this section we want to obtain a relation between the dipole operators and the electric field as it's demonstrated in [15].
Mathematically, the Hamiltonian describing the system of one quantum emitter coupled to an electromagnetic field is

$$H = H_0 + H_{\mathrm{Int}} + H_{\mathrm{F}}. \tag{2.1}$$

The free energy Hamiltonian is

$$H_0 = \hbar\omega_0 \ \sigma^+\sigma^- \tag{2.2}$$

with $\sigma^- = |g\rangle \langle e|$ being the transition operator from the excited state $|e\rangle$ to the ground state $|g\rangle$ of the atom with transition frequency $\omega_0 = c\,|k_0|$. The interaction Hamiltonian coupling the electric field $\vec{E}(0,t)$ and the dipole $\vec{d}$ is given by

$$H_{\mathrm{Int}} = \vec{d}\,\vec{E}(0,t) = \vec{\mu}\ (\sigma^+ + \sigma^-)\ \vec{E}(0,t). \tag{2.3}$$

where the atom is treated in the dipole-approximation. The electric field can be split up into forward and backward propagating fields as [16]

$$\vec{E}(\vec{r},t) = \vec{E}^+(\vec{r},t) + \vec{E}^-(\vec{r},t). \tag{2.4}$$

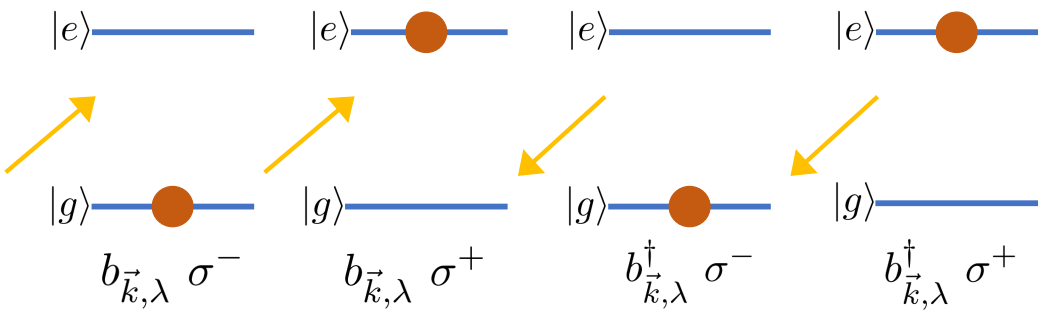

Figure 2.1: *Occurring processes.* When a light field interacts with a two-level quantum emitter with resonance frequency $\hbar\omega_0$, there are four possible processes that can occur in the dipole-approximation. Two of them ($b_{\vec{k},\lambda}\ \sigma^+$ and $b^\dagger_{\vec{k},\lambda}\ \sigma^-$) are energy-conserving and therefore we keep them in the rotating-wave approximation. The other two interactions ($b_{\vec{k},\lambda}\ \sigma^-$ and $b^\dagger_{\vec{k},\lambda}\ \sigma^+$) are neglected.

For further calculations it's convenient to expand the field embedded in a box with spatial volume $V = L^3$ in the Heisenberg picture in a mode expansion

$$\vec{E}(\vec{r},t) = \sum_{\vec{k},\lambda} \sqrt{\frac{\hbar\omega_k}{2\epsilon_0 V}}\ \vec{e}_{\vec{k},\lambda}\ \mathrm{e}^{i\vec{k}\vec{r}}\ b_{\vec{k},\lambda}(t) \tag{2.5}$$

assuming that there are no external sources and periodic boundary conditions. There are infinitely many field modes with wave vector $\vec{k}$, frequency ω_k and polarizations $\lambda \in [1,2]$. The polarization unit vector is then given by $\vec{e}_{\vec{k},\lambda}$. With the time-dependent annihilation and creation operators $b_{\vec{k},\lambda}$ and $b^\dagger_{\vec{k},\lambda}$ fulfilling the canonical commutation relations, i.e, $[b_{\vec{k},\lambda}, b^\dagger_{\vec{k}',\lambda'}] = \delta_{\vec{k},\vec{k}'}\delta_{\lambda,\lambda'}$, one can define the field Hamiltonian as

$$H_\mathrm{F} = \sum_{k,\lambda} \hbar\omega_k\ b^\dagger_{\vec{k},\lambda} b_{\vec{k},\lambda}. \tag{2.6}$$

In the *Rotating-Wave-Approximation* (RWA), where non-energy-conserving interactions are neglected as visualized in Fig. 2.1, the full Hamiltonian H of the system is

$$H = \hbar\omega_0\ \sigma^+\sigma^- + \sum_{\vec{k},\lambda} \hbar\omega_k\ b^\dagger_{\vec{k},\lambda} b_{\vec{k},\lambda} + \sum_{\vec{k},\lambda} \hbar g_{\vec{k},\lambda}(\sigma^+ b_{\vec{k},\lambda} + b^\dagger_{\vec{k},\lambda}\sigma^-) \tag{2.7}$$

with the coupling constant $g_{\vec{k},\lambda} = \sqrt{\frac{\omega_k}{2\hbar\epsilon_0 V}}\ \vec{e}_{\vec{k},\lambda}\ \vec{\mu}$. In the next step we want to extend our model to the case of N identical coupled quantum emitters following the procedure of [17]. The Hilbertspace of the emitters is of dimension $2^{\otimes N}$ and the emitter operator taking us from the ground to the excited state of the first atom is $\sigma_1^+ \otimes \mathbb{1}_2 \otimes ... \otimes \mathbb{1}_N$. The Hamiltonian takes the form

$$H = \hbar\omega_0 \sum_j \sigma_j^\dagger\sigma_j + \sum_{\vec{k},\lambda} \hbar\omega_k\ b^\dagger_{\vec{k},\lambda} b_{\vec{k},\lambda} + \sum_{\vec{k},\lambda}\sum_j \hbar g^{(j)}_{\vec{k},\lambda} \left(\sigma_j^+ b_{\vec{k},\lambda}\ \mathrm{e}^{i\vec{k}\vec{r}_j} + b^\dagger_{\vec{k},\lambda}\sigma_j\ \mathrm{e}^{-i\vec{k}\vec{r}_j}\right). \tag{2.8}$$

The coupling strength of the j-th emitter is $g^{(j)}_{\vec{k},\lambda} = \sqrt{\frac{\omega_k}{2\hbar\epsilon_0 V}}\ \vec{e}_{\vec{k},\lambda}\ \vec{\mu}_j$. As we assume to have identical quantum emitters, $|\vec{\mu}_j| = |\vec{\mu}|$ applies for the dipole vectors. The creation and annihilation operators

fulfill the Heisenberg equation of motion

$$\dot{b}_{\vec{k},\lambda} = \frac{i}{\hbar}[H, b_{\vec{k},\lambda}] = -i\omega_k \; b_{\vec{k},\lambda} - i\sum_j g^{(j)}_{\vec{k},\lambda} \; \mathrm{e}^{-i\vec{k}\vec{r}_j}\sigma^-_j \tag{2.9}$$

where the first term accounts for the free radiation field and the second term including the time-dependent source term σ^-_j is called the quantum current. One obtains a solution to this equation via integration with the retarded Green's function, i.e

$$b_{\vec{k},\lambda}(t) = b_{\vec{k},\lambda}(0) \; \mathrm{e}^{-i\omega_k t} - i\sum_j g^{(j)}_{\vec{k},\lambda} \; \mathrm{e}^{-i\vec{k}\vec{r}_j} \int_0^t \sigma_j(t') \; \mathrm{e}^{i\omega_k(t'-t)} \; \mathrm{d}t'. \tag{2.10}$$

The time-dependent annihilation operator is then dependent on the emitter operators at previous times $t' < t$. Inserting this into Eq. (2.5), both, the forward and backward propagating fields are again made up of two terms each. The forward propagating field is

$$\vec{E}^+(\vec{r},t) = \vec{E}^+_{\mathrm{in}}(\vec{r},t) + \vec{E}^+_0(\vec{r},t). \tag{2.11}$$

Here, the free evolution of the initial electric field is given by

$$\vec{E}^+_{\mathrm{in}}(\vec{r},t) = \sum_{\vec{k},\lambda} \sqrt{\frac{\hbar\omega_k}{2\epsilon_0 V}} \; \vec{e}_{\vec{k},\lambda} \; \mathrm{e}^{i\vec{k}\vec{r}} \; b_{\vec{k},\lambda}(0) \; \mathrm{e}^{-i\omega_k t}. \tag{2.12}$$

As we assume to have vacuum initially and $\vec{E}^+_{\mathrm{in}}(\vec{r},t)\,|\Psi(t=0)\rangle = 0$, respectively, we neglect this term although it gives rise to quantum noise.
In order to solve the integral in Eq. (2.10) we use the so-called *Markov-Approximation* that gives rise to the simplification

$$\begin{aligned} &\sigma^-_i(t) \propto \sigma^-_i(0) \; \mathrm{e}^{-i\omega_0 t}, \quad s^-_i(t) = \sigma^-_i(t) \; \mathrm{e}^{i\omega_0 t} \propto \sigma^-_i(0) \\ &\int_0^t \mathrm{d}t' \sigma^-_i(t') = s^-_i(t) \int_0^t \mathrm{d}t' \mathrm{e}^{-i\omega_0 t'} = \sigma^-_i(t) \int_0^t \mathrm{e}^{-i\omega_0(t'-t)}. \end{aligned} \tag{2.13}$$

It is applicable as we already assumed within the RWA that the resonance frequency of the emitter transition is dominant in the radiation field. Now you can insert this into Eq. (2.10) and you obtain

$$E^+_0(\vec{r},t) = -i\sum_{\vec{k},\lambda}\sum_j \sqrt{\frac{\hbar\omega_k}{2\epsilon_0 V}} \; \vec{e}_{\vec{k},\lambda} \; g^{(j)}_{\vec{k},\lambda} \; \mathrm{e}^{i\vec{k}(\vec{r}-\vec{r}_j)} \sigma^-_j(t) \int_0^t \mathrm{d}t' \mathrm{e}^{i(\omega_k-\omega_0)(t'-t)}. \tag{2.14}$$

For a fully simplified form you take advantage of the fact that $\vec{e}_{\vec{k},\lambda}$ and $\vec{k}$ form an orthonormal basis. Furthermore we assume that we have a high density of modes in the radiation field that allows us to replace the sum over all modes $\vec{k}$ with an integral. Ultimately, after some transformations, we obtain the relation between the electric field and the dipole operators

$$\vec{E}^+(\vec{r},t) = \vec{E}^+_{\mathrm{in}}(\vec{r},t) - \frac{3\hbar\Gamma_0}{4|\vec{\mu}|} \sum_j \sigma^-_j(t) \; \mathcal{G}(k_0, \vec{r}-\vec{r}_j) \; \hat{\vec{\mu}}_j. \tag{2.15}$$

The spontaneous emission rate of a single quantum emitter is $\Gamma_0 = \frac{\omega_0^3|\vec{\mu}|^2}{3\pi c^3\epsilon_0\hbar}$ and the Green's Tensor is defined via

$$\mathcal{G}(k,\vec{r}) = \mathrm{e}^{ikr}\left[\left(\frac{1}{kr} + \frac{i}{(kr)^2} - \frac{1}{(kr)^3}\right)\mathbb{1} - (\,\hat{\vec{r}} \circ \hat{\vec{r}}\,)\left(\frac{1}{kr} + \frac{3i}{(kr)^2} - \frac{3}{(kr)^3}\right)\right] \tag{2.16}$$

with $\hat{\vec{r}} = \frac{\vec{r}}{|\vec{r}|}$ and $\circ$ denoting the dyadic product. The radiated intensity reads

$$\vec{I}(\vec{r},t) = \langle \vec{E}^-(\vec{r},t) \cdot \vec{E}^+(\vec{r},t) \rangle. \tag{2.17}$$

2.2 Dipole-Dipole Interactions

In the previous section a relation between the electric fields and the atomic dipole operators is derived. This expression provides information about the full dynamics of the system. We see that the momentary electric field, mediating the interactions, directly depends on the atomic state. Hence in the next step we want to find a simplified description of the dynamics without explicit use of the electric field but providing the same information about the system. If needed we can later evaluate the field at any time from the current atomic state.

2.2.1 Quantum Langevin Equations for the Open Atomic Dynamics

We start out with the evolution of an arbitrary emitter operator O that commutes with b and $b^\dagger$ at equal time. The Hamiltonian that is in charge of the time evolution of the operator O in the Heisenberg picture is made up of the free energy Hamiltonian H_0 defined in Eq. (2.2) and the Interaction Hamiltonian for N identical quantum emitters in the Rotating Wave Approximation

$$H_{\text{Int}} = \sum_j (\sigma_j^+ (\vec{\mu}_j \cdot \vec{E}^+(\vec{r}_j))) + ((\vec{\mu}_j \cdot \vec{E}^-(\vec{r}_j))\ \sigma_j^-). \tag{2.18}$$

The evolution is governed by the Heisenberg equation of motion

$$\begin{aligned} \dot{O} &= \frac{i}{\hbar}[H, O] = \frac{i}{\hbar}[H_0 + H_{\text{Int}}, O] = \\ &= \frac{i}{\hbar}[H_0, O] + \frac{i}{\hbar}\sum_j \Big[[\sigma_j^+, O](\vec{\mu}_j \cdot \vec{E}^+(\vec{r}_j)) + (\vec{\mu}_j \cdot \vec{E}^-(\vec{r}_j))[\sigma_j^-, O] \Big]. \end{aligned} \tag{2.19}$$

Now you can insert the electric field given by Eq. (2.15) and the term including the forward electric fields in Eq. (2.19) becomes

$$\frac{i}{\hbar}\sum_k [\sigma_k^+, O] \left(\vec{\mu}_k \cdot \vec{E}_{\text{in}}^+(\vec{r}_k) - \frac{3\hbar\Gamma_0}{4} \sum_j \sigma_j^-(t)\ \hat{\vec{\mu}}_k \cdot \mathcal{G}(k_0, \vec{r}_k - \vec{r}_j) \cdot \hat{\vec{\mu}}_j \right). \tag{2.20}$$

Splitting the Green's Tensor into real and imaginary part and defining $\vec{r}_{kj} = \vec{r}_k - \vec{r}_j$ you arrive at

$$\begin{aligned} \sum_k [\sigma_k^+, O] \ \Big[&\frac{i}{\hbar}\ \vec{\mu}_k \cdot \vec{E}_{\text{in}}^+(\vec{r}_k) - \frac{3i\Gamma_0}{4} \sum_j \sigma_j^- \hat{\vec{\mu}}_k \cdot \Re(\mathcal{G}(k_0, \vec{r}_{kj})) \cdot \hat{\vec{\mu}}_j \ + \\ &+ \frac{3\Gamma_0}{4} \sum_j \sigma_j^- \hat{\vec{\mu}}_k \cdot \Im(\mathcal{G}(k_0, \vec{r}_{kj})) \cdot \hat{\vec{\mu}}_j \Big]. \end{aligned} \tag{2.21}$$

On the other hand for the backward fields part in Eq. (2.19) you obtain

$$\begin{aligned} \sum_k \Big[&\frac{i}{\hbar}\ \vec{\mu}_k \cdot \vec{E}_{\text{in}}^-(\vec{r}_k) - \frac{3i\Gamma_0}{4} \sum_j \sigma_j^+ \hat{\vec{\mu}}_k \cdot \Re(\mathcal{G}(k_0, \vec{r}_{kj})) \cdot \hat{\vec{\mu}}_j \ - \\ &- \frac{3\Gamma_0}{4} \sum_j \sigma_j^+ \hat{\vec{\mu}}_k \cdot \Im(\mathcal{G}(k_0, \vec{r}_{kj})) \cdot \hat{\vec{\mu}}_j \Big] [\sigma_k^-, O]. \end{aligned} \tag{2.22}$$

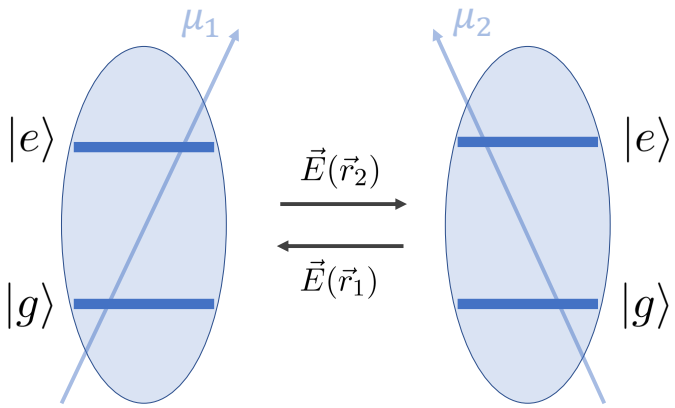

Figure 2.2: *Dipole interaction.* Schematic picture of two identical two-level quantum emitters with dipoles $\vec{\mu}_1$ and $\vec{\mu}_2$ coupled to the electric fields $\vec{E}(\vec{r})$ at positions $\vec{r}_1$ and $\vec{r}_2$. The transition frequency from the ground to the excited state is $\hbar\omega_0$ in both atoms.

where the minus sign of the last term accounts for the complex conjugate of the Green's Tensor in backwards fields $\vec{E}^-(\vec{r}_k)$. Putting everything together, Eq. (2.19) becomes

$$\begin{aligned}\dot{O} = \frac{i}{\hbar}[H_0, O] - \frac{3i\Gamma_0}{4}\sum_{k,j}[\sigma_k^+\sigma_j^-, O]\left(\hat{\vec{\mu}}_k \cdot \Re(\mathcal{G}(k_0, \vec{r}_{kj})) \cdot \hat{\vec{\mu}}_j\right) + \\ + \sum_k [\sigma_k^+, O]\left[\frac{i}{\hbar}\,\vec{\mu}_k \cdot \vec{E}^+_{\text{in}}(\vec{r}_k) + \frac{3\Gamma_0}{4}\sum_j\left(\hat{\vec{\mu}}_k \cdot \Im(\mathcal{G}(k_0, \vec{r}_{kj})) \cdot \hat{\vec{\mu}}_j\right)\sigma_j\right] + \\ + \sum_k \left[\frac{i}{\hbar}\,\vec{\mu}_k \cdot \vec{E}^-_{\text{in}}(\vec{r}_k) - \frac{3\Gamma_0}{4}\sum_j\left(\hat{\vec{\mu}}_k \cdot \Im(\mathcal{G}(k_0, \vec{r}_{kj})) \cdot \hat{\vec{\mu}}_j\right)\sigma_j^+\right][\sigma_k^-, O].\end{aligned} \tag{2.23}$$

For simplification we define the *quantum noise operators*

$$\xi_j^-(t) := \frac{i}{\hbar\sqrt{\Gamma_0}}\,(\vec{\mu}_j\ \vec{E}^+_{\text{in}}(\vec{r}_j, t)) = \frac{i}{\sqrt{\Gamma_0}}\sum_{\vec{k},\lambda} g^{(j)}_{\vec{k},\lambda}\ a_{\vec{k},\lambda}(0)\ \mathrm{e}^{-i\omega_k t}\ \mathrm{e}^{i\vec{k}\vec{r}_j} \tag{2.24}$$

that fulfill the canonical commutation relation and two-time correlation function, respectively,

$$[\xi_m(t), \xi_n^\dagger(t')] \approx \frac{3}{2}\ \delta(t-t')\ \hat{\vec{\mu}}_m \cdot \Im(\mathcal{G}(k_0, \vec{r}_{mn})) \cdot \hat{\vec{\mu}}_n. \tag{2.25}$$

Finally you arrive at the *Quantum Langevin Equation* for N coupled identical quantum emitters

$$\begin{aligned}\dot{O} = \frac{i}{\hbar}[H_0 + H_{\text{dip}}, O] + \sum_{j,k}[\sigma_j^+, O](\delta_{jk}\ \sqrt{\Gamma_0}\ \xi_j^-(t) + \frac{\Gamma_{jk}}{2}\sigma_k) - \\ - \sum_{j,k}(\delta_{jk}\sqrt{\Gamma_0}\ \xi_j^+(t) + \frac{\Gamma_{jk}}{2}\sigma_k^+)[\sigma_j, O],\end{aligned} \tag{2.26}$$

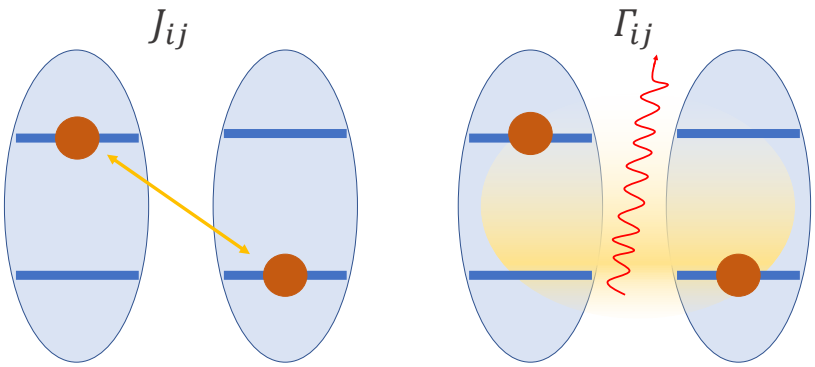

Figure 2.3: *Schematic picture of collective energy-shifts and decay rates in two coupled, identical two-level quantum emitters.*

where we assume that $\omega_k \approx \omega_0$. Moreover we defined the Dipole Hamiltonian as

$$H_{\text{dip}} = \sum_{j,k} \hbar J_{jk} \sigma_j^+ \sigma_k^- \tag{2.27}$$

with the coherent coupling

$$J_{ij} = -\frac{3\Gamma_0}{4} \hat{\vec{\mu}}_i \cdot \Re(\mathcal{G}(k_0, \vec{r}_{ij})) \cdot \hat{\vec{\mu}}_j \tag{2.28}$$

and we introduced the collective decay rates

$$\Gamma_{ij} = \frac{3\Gamma_0}{2} \hat{\vec{\mu}}_i \cdot \Im(\mathcal{G}(k_0, \vec{r}_{ij})) \cdot \hat{\vec{\mu}}_j. \tag{2.29}$$

These can also be written in a simpler form

$$J_{ij} = \Gamma_0 \; G(k_0, r_{ij}) \quad \Gamma_{ij} = \Gamma_0 \; F(k_0, r_{ij}) \tag{2.30}$$

by defining

$$\begin{aligned} G(\xi) &= -\frac{3}{4} \left[(1 - \cos^2\theta) \; \frac{\cos\xi}{\xi} - (1 - 3\cos^2\theta) \; \left(\frac{\sin\xi}{\xi^2} + \frac{\cos\xi}{\xi^3} \right) \right] \\ F(\xi) &= \frac{3}{2} \left[(1 - \cos^2\theta) \; \frac{\sin\xi}{\xi} - (1 - 3\cos^2\theta) \; \left(\frac{\cos\xi}{\xi^2} - \frac{\sin\xi}{\xi^3} \right) \right] \end{aligned} \tag{2.31}$$

with the unit vectors of the dipoles and positions fulfilling $\cos\theta = \vec{e}_{\vec{\mu}} \cdot \vec{e}_{\vec{r}_{ij}}$.

The behaviour of these two collective parameters, both plotted in Fig. 2.4, in special limits are of interest. In the Dicke limit [7], where $r_{ij} \to 0$ and the distance between the atoms is much smaller than the interaction range, respectively, the collective energy-shifts J_{ij} diverge whereas the collective decay rates approach the single emitter decay rate Γ_0, i.e., $\Gamma_{ij} \to \Gamma_0$. In order to circumvent the divergence in the collective energy-shifts, we fix $J_{ii} = 0$. In the limit of $r_{ij} \to \infty$, the distance between the atoms is so large, the emitters effectively behave as single uncoupled quantum emitters meaning that $J_{ij} \to 0$ and $\Gamma_{ij} \to \Gamma_0 \; \delta_{ij}$.

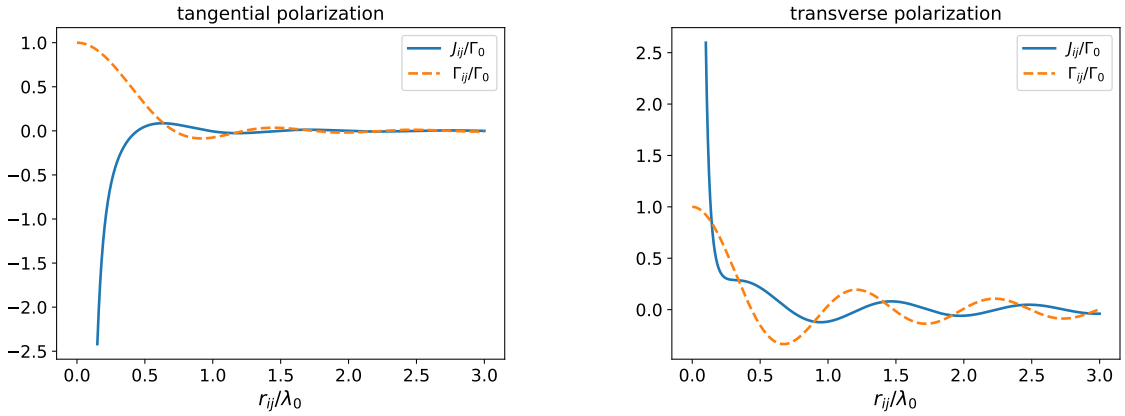

(a) (b)

Figure 2.4: *Interaction induced pairwise atomic coupling.* The real part of the eigenvalues, i.e., the energy-shifts J_{ij} and the imaginary part of the eigenvalues, i.e., the decay rates Γ_{ij} of the dipole-dipole coupling strength are plotted as function of the distances r_{ij} between the atoms for **(a)** tangential and **(b)** transverse polarization.

2.2.2 Master Equation

The Quantum Langevin Equations describe the dynamics of the open atom-field system in the Heisenberg picture. Thus, our operators are time-dependent. In some cases solving this equation turns out to be difficult. However, switching to the Schroedinger picture, i.e., dealing with the time-dependent mixed state in the atomic density matrix $\rho(t)$, we arrive at a Master Equation, which provides the same information and is simpler to solve in particular instances.
The goal of this section is to arrive at this kind of equation that describes the evolution of the state $\rho(t)$ of the emitters in time assuming that there are no correlations at time $t = 0$. With the collective initial state of emitters and fields $\rho(0) \otimes \rho_{\mathrm{F}}(0)$ one can write the state of the emitters at time t as $\rho(t) = \mathrm{tr}_{\mathrm{F}}\{U(t)\rho(0) \otimes \rho_{\mathrm{F}}(0)U^{\dagger}(t)\}$. $U(t)$ is the unitary evolution operator $U(t) = \exp(-iHt/\hbar)$ with the Hamiltonian defined in Eq. (2.8). Making use of the property

$$\mathrm{tr}\{O(t)\rho(0) \otimes \rho_{\mathrm{F}}(0)\} = \mathrm{tr}\{O(0)\rho(t)\} \tag{2.32}$$

the time-derivative turns out to be

$$\mathrm{tr}\{\dot{O}(t)\rho(0) \otimes \rho_{\mathrm{F}}(0)\} = \mathrm{tr}\{O(0)\dot{\rho}(t)\}. \tag{2.33}$$

Then you insert the Quantum Langevin Equation from Eq. (2.26) and by comparing you obtain the Master equation for N-coupled identical quantum emitters

$$\dot{\rho} = -\frac{i}{\hbar}[H_0 + H_{\mathrm{dip}}, \rho] + \mathcal{L}[\rho] \tag{2.34}$$

with the Lindblad term

$$\mathcal{L}[\rho] = \sum_{i,j} \frac{\Gamma_{ij}}{2} \left(2\sigma_i^- \rho \sigma_j^+ - \sigma_i^+ \sigma_j^- \rho - \rho \sigma_i^+ \sigma_j^-\right) \tag{2.35}$$

and the dipole Hamiltonian H_{dip} defined in Eq. (2.27).

2.3 Sub- and Superradiance

A single excited atom in free space decays to the ground state at a fixed rate Γ following an exponential law. Super- and subradiance are phenomena of enhanced or suppressed spontaneous emission that arise from constructive and, respectively, destructive interference of the emitted light. Here we will have a closer look at the theoretical description restricting us to the case of two dipole-coupled two-level quantum emitters. This section is based on the discussions and calculations of Laurin Ostermann in his thesis [18]. We start out with the bare atomic states

$$\{|gg\rangle \equiv |g\rangle \otimes |g\rangle\,, |ge\rangle \equiv |g\rangle \otimes |e\rangle\,, |eg\rangle \equiv |e\rangle \otimes |g\rangle\,, |ee\rangle \equiv |e\rangle \otimes |e\rangle\} \tag{2.36}$$

where the first (second) Hilbertspace corresponds to the first (second) atom. The Hamiltonian describing the system is

$$H = \omega_0(\sigma_1^+\sigma_1^- + \sigma_2^+\sigma_2^-) + J(\sigma_1^+\sigma_2^- + \sigma_1^-\sigma_2^+) \tag{2.37}$$

where the coherent coupling is given by $J = \Gamma_0\ G(k_0, r)$ (cf. Eq. (2.30)). Its eigenstates are obtained through diagonalization and are

$$\begin{aligned} |G\rangle &= |gg\rangle \\ |S\rangle &= \frac{1}{\sqrt{2}}(|eg\rangle + |ge\rangle) \\ |A\rangle &= \frac{1}{\sqrt{2}}(|eg\rangle - |ge\rangle) \\ |E\rangle &= |ee\rangle\,. \end{aligned} \tag{2.38}$$

Choosing a suitable transformation for the eigenstates as it's done in [18], we're able to write the Lindblad term as

$$\mathcal{L}[\rho] = \mathcal{L}_\mathrm{S}[\rho] + \mathcal{L}_\mathrm{A}[\rho]. \tag{2.39}$$

In this representation of the Lindblad term we define two different collective decay rates given by

$$\begin{aligned} \Gamma_\mathrm{S} &= \Gamma_0 + \Gamma \\ \Gamma_\mathrm{A} &= \Gamma_0 - \Gamma \end{aligned} \tag{2.40}$$

with the collective decay rate $\Gamma = \Gamma_0\ F(k_0, r)$ (cf. Eq. (2.30)). For $\Gamma > 0$, the channel including the symmetric state $|S\rangle$ possesses a higher decay rate than the single atom decay rate Γ_0 and thus, it is called *superradiant* channel. On the other hand, the decay rate of the channel including the anti-symmetric state $|A\rangle$ is decreased and therefore it is called *subradiant*.

Chapter 3

Single Ring Structures

As noted above the presence of other emitters changes the dynamics of spontaneous emission. As a central example we review here the corresponding properties of a single ring of dipole-dipole coupled two-level atoms in the single-excitation manifold.

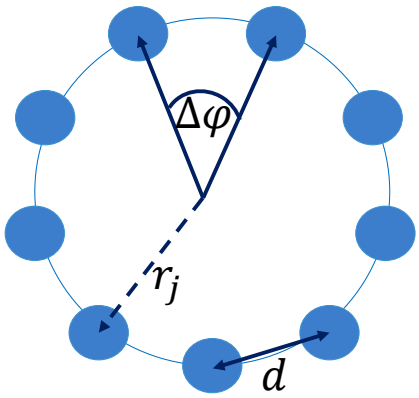

Figure 3.1: *Single ring configuration.* The sub-wavelength-spaced quantum emitters are equally distributed on the ring with an angle $\Delta\phi$ between them and inter-particle distance d. The position vector r_j corresponds to the quantum emitter at site j. The number of atoms is N.

3.1 Model

A single ring of N two-level atoms is depicted in Fig. 3.1 with the geometric ring-parameters, such as the distance between the emitters d or the position vector r_j of the j-th atom in the ring. The atoms are equally distributed over the ring with an angle $\Delta\phi = \frac{2\pi}{N}$ in between. Thus, the angle $\phi(j)$ corresponding to the position of the j-th atom is

$$\phi(j) = \frac{2\pi(j-1)}{N}. \tag{3.1}$$

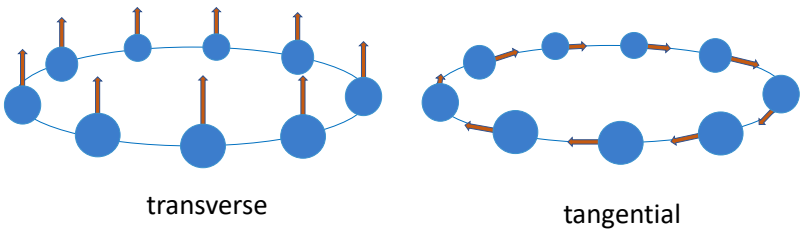

Figure 3.2: *Schematic picture of transverse and tangential dipole orientation.*

Having these parameters one can calculate the radius of the ring via

$$R(d) = \frac{d}{2\sin(\Delta\phi/2)}. \tag{3.2}$$

The position vectors are defined in cylindrical coordinates. In the following, we will mostly focus on rings with $N = 9$ atoms. The orientation of the dipoles can be either transverse or tangential, as schematically illustrated in Fig. 3.2. In our case, the unit dipole vectors for transverse and tangential polarization are given in cartesian coordinates by

$$\hat{\vec{\mu}}_{\text{transv},j} = \begin{bmatrix} 0 \\ 0 \\ 1 \end{bmatrix}, \quad \hat{\vec{\mu}}_{\text{tangen},j} = \begin{bmatrix} -\sin\phi(j) \\ \cos\phi(j) \\ 0 \end{bmatrix}. \tag{3.3}$$

We restrict our analysis to the single excitation manifold which allows us to describe the system in terms of an effective non-Hermitian Hamiltonian. In order to do so we start out with Eq. (2.34) and neglect the so-called *recycling term* $2\sigma_j^-\rho(t)\sigma_k^+ = |g\rangle\langle e_j|\rho|e_k\rangle\langle g| = \rho_{ee}^{jk}|g\rangle\langle g|$, as it only modifies the ground state population and it does not affect the observables of interest, such as the radiated fields . The master equation reads

$$\begin{aligned}
\dot{\rho} &= -i[H_{\text{dip}},\rho] + \mathcal{L}[\rho] = \\
&= -i\Big\{[H_{\text{dip}},\rho] - i\sum_{j,k}\frac{\Gamma_{jk}}{2}(-\sigma_j^+\sigma_k^-\rho - \rho\sigma_j^+\sigma_k^-)\Big\} = \\
&= -i\Big\{[H_{\text{dip}},\rho] - i\sum_{j,k}\frac{\Gamma_{jk}}{2}\{\sigma_j^+\sigma_k^-,\rho\}\Big\} = \\
&= -i[H_{\text{eff}},\rho]
\end{aligned} \tag{3.4}$$

with the effective non-hermitian Hamiltonian

$$H_{\text{eff}} = \sum_{j,k}\left(J_{jk} - i\frac{\Gamma_{jk}}{2}\right)\sigma_j^+\sigma_k^- \equiv \sum_{j,k} G_{jk}\,\sigma_j^+\sigma_k^-. \tag{3.5}$$

Here we defined $G_{jk} = J_{jk} - i\frac{\Gamma_{jk}}{2}$.

3.2 Analytical Diagonalization of the Effective Hamiltonian

The aim of this section is to analytically diagonalize the effective Hamiltonian from Eq. (3.5). A *spin-wave Ansatz*

$$\sigma_i^+ = \frac{1}{\sqrt{N}}\sum_m \mathrm{e}^{im\phi_i}\tilde{\sigma}_m^+ \tag{3.6}$$

and effectively a Fourier Transformation, respectively, can be chosen in order to obtain a diagonal Hamiltonian. In this Ansatz the excitation is considered as a running wave on the ring with angular momentum m with $m = 0, \pm1, \pm2, \cdots, \lceil \pm(N-1)/2 \rceil$, where $\lceil \cdot \rceil$ is the ceiling function.

Inserting the Ansatz into Eq. (3.5) you get

$$\begin{aligned} H_{\text{eff}} &= \sum_{i,j} G_{ij} \sigma_i^+ \sigma_j^- = \frac{1}{N} \sum_{i,j} \sum_{m,m'} G_{ij} \mathrm{e}^{-im\phi_i} \mathrm{e}^{im'\phi_j} \tilde{\sigma}_m^+ \tilde{\sigma}_{m'}^- = \\ &= \frac{1}{N} \sum_{i,j} G_{ij} \sum_{m,m'} \mathrm{e}^{im(\phi_j - \phi_i)} \mathrm{e}^{i(m'-m)\phi_j} \tilde{\sigma}_m^+ \tilde{\sigma}_{m'}^- = \\ &= \frac{1}{N} \sum_{i,j} G_{ij} \sum_{m,m'} \mathrm{e}^{im\Delta\phi(j-i)} \mathrm{e}^{i(m'-m)\Delta\phi j} \tilde{\sigma}_m^+ \tilde{\sigma}_{m'}^-. \end{aligned} \tag{3.7}$$

In the next step we take advantage of the rotational symmetry in the single ring and can combine $\sum_i G_{ij} \mathrm{e}^{im\Delta\phi(j-i)}$ to an object G_m that is independent of i and j. This can be seen easily by studying the sum

$$\sum_i G_{ij} \mathrm{e}^{im\frac{2\pi}{N}(j-i)} = G_{1j} \mathrm{e}^{im\frac{2\pi}{N}(j-1)} + G_{2j} \mathrm{e}^{im\frac{2\pi}{N}(j-2)} + ... + G_{Nj} \mathrm{e}^{im\frac{2\pi}{N}(j-N)} \tag{3.8}$$

for different values of j. For $j = 1$ this results in

$$\begin{aligned} ... &= G_{11} \mathrm{e}^{im\frac{2\pi}{N}\ 0} + g_{21} \mathrm{e}^{im\frac{2\pi}{N}(-1)} + ... + G_{N1} \mathrm{e}^{im\frac{2\pi}{N}(-N+1)} \\ &= G_{11} + G_{21} \mathrm{e}^{-im\frac{2\pi}{N}} + ... + G_{N1} \mathrm{e}^{im\frac{2\pi}{N}}, \end{aligned} \tag{3.9}$$

while Eq. (3.8) gives rise to

$$... = G_{1N} \mathrm{e}^{-im\frac{2\pi}{N}} + ... + G_{(N-1)N} \mathrm{e}^{im\frac{2\pi}{N}} \tag{3.10}$$

for $j = N$. By symmetry considerations it holds that $G_{11} = ... = G_{NN}$, $G_{N1} = G_{12} = G_{23} = ...$, $G_{1N} = G_{21} = ...$ and $G_{13} = G_{24} = G_{N2}$ and so forth. Now, having a look at Eq. (3.8) again, you see that each part gives rise to an equal expression. Consequently Eq. (3.8) is indeed only depending on the angular momentum quantum number m and we can write it as $\sum_i G_{ij} \mathrm{e}^{im\Delta\phi(j-i)} = NG_m$. Coming back to our original effective Hamiltonian from Eq. (3.7) we can continue

$$H_{\text{eff}} = \frac{1}{N^2} \sum_j \sum_{m,m'} G_m \mathrm{e}^{i(m'-m)\Delta\phi j} \tilde{\sigma}_m^+ \tilde{\sigma}_{m'}^-. \tag{3.11}$$

The sum over j collapses into a delta function by considering

$$\sum_j \mathrm{e}^{i(m'-m)\Delta\phi j} = \sum_j \mathrm{e}^{i(m'-m)\frac{2\pi}{N} j} = \sum_j \mathrm{e}^{in\frac{2\pi}{N}}. \tag{3.12}$$

If $n \neq 0$ this whole sum gives zero and otherwise you get N. Thus, one can write

$$\frac{1}{N} \sum_j \mathrm{e}^{i(m'-m)\Delta\phi j} = \delta_{m,m'}. \tag{3.13}$$

In this way we achieved a diagonal form of our Hamiltonian, i.e.,

$$H_{\text{eff}}^{\text{diag}} = \sum_m G_m\ \tilde{\sigma}_m^+ \tilde{\sigma}_m^- = \sum_m \lambda_m\ \tilde{\sigma}_m^+ \tilde{\sigma}_m^-. \tag{3.14}$$

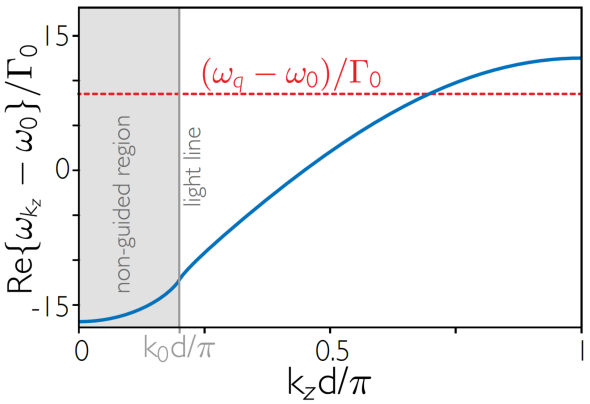

Figure 3.3: *Dispersion Relation of an infinite, 1D chain in the single-excitation manifold with distance $d = 0.1\lambda_0$ between the atoms.* In the shaded region, i.e., $|k_z| \leq k_0$, the spin-waves have a finite life-time [19] and decay into free space via photon emission. For $|k_z| \geq k_0$, the modes are guided as the decay rate of the spin-waves is zero. In this case the chain behaves as a waveguide. The light line is the boundary line between those two regions. The plot is extracted from [19].

The corresponding eigenvalues are then given by

$$\lambda_m = -\frac{3\pi\Gamma_0}{Nk_0} \sum_{j,l} \mathrm{e}^{im(\phi_l - \phi_j)}\ G_{jl}. \tag{3.15}$$

They give rise to the collective energy-shifts

$$J_\mathrm{m} = \Re(\lambda_\mathrm{m}) \tag{3.16}$$

and the collective decay rates

$$\Gamma_\mathrm{m} = -2\ \Im(\lambda_m). \tag{3.17}$$

The eigenstates are

$$|\Psi_m\rangle = \frac{1}{\sqrt{N}} \sum_j \mathrm{e}^{im\phi_j}\ \sigma_j^+ |G\rangle \tag{3.18}$$

where $|G\rangle = |g\rangle_1 \otimes |g\rangle_2 \otimes ... \otimes |g\rangle_N$ is the absolute ground state of the system.

3.3 Dispersion Relation, Light Line and Collective Emission

In free space photon energy is linearly connected to its wave-vector and the dispersion relation corresponding to light propagation in free space can be used to define the so called light line for dipole arrays. In Fig. 3.3 the dispersion relation of an infinite chain of atoms with well-defined wave-vector $k_\mathrm{z} \in [-\pi/d, +\pi/d]$ is depicted. The shaded region in Fig. 3.3 is called the non-guided region. The modes decay into free space due to photon emission. The non-shaded region is called the guided region. Here the linear momentum of the spin-waves is higher than the one of the surrounding vacuum k_0 and the excitons can no longer couple to free space. Thus, spontaneous emission is suppressed and the decay rate is zero, i.e., you obtain perfect subradiance.

The collective decay rate[1], of a ring is plotted as a function of the well-defined angular momentum m and can be directly compared to the dispersion relation of an infinite chain of emitters (cf. Fig. 3.3) via

$$\frac{2m}{N} = \frac{k_m d}{\pi} \tag{3.19}$$

in the limit of $N \to \infty$. Setting $k_m = k_0 = 2\pi/\lambda$ one gets

$$\frac{m}{N} = d/\lambda. \tag{3.20}$$

This is the position of the light line. In a ring configuration consisting of N quantum emitters you have $|m| = N$ modes with well-defined angular momentum $m \in \left[-\frac{N-1}{2}, \frac{N-1}{2}\right]$. The maximal value is $m = \frac{N-1}{2}$. Consequently we obtain the relation

$$\frac{d}{\lambda} = \frac{N-1}{2N} < \frac{1}{2}. \tag{3.21}$$

This tells us that the position of the light line is at $2m_{\text{ll}}/N = 2d$. Thus, if $\frac{2m}{N}$ is larger than $2d/\lambda$, the modes are subradiant as their linear moment is larger than the one of the surrounding space. On the other hand, if the distance between the emitters d/λ is larger than $1/2$, there are no subradiant modes.
In fact, this discussion is based on the assumption that a circle with an increasing radius and decreasing curvature, respectively, approaches an infinite chain for $N \to \infty$. Consequently, there might occur deviations in the following discussions due to the finite size of the rings.

3.3.1 Collective Eigenmodes and Decay Rates

In Fig. 3.4 the collective decay rate of a single ring configuration is plotted for two different distances between the emitters as a function of the normalized angular momentum $\frac{2m}{N}$. The behaviour of the decay rates is opposite for transverse and tangential polarization within the non-guided region. For tangential dipole orientation and $d/\lambda = 1/3$, $m = 0$ is the superradiant mode whereas in the case of transverse polarization modes close to the light line are superradiant. However, in this case, also the $m = 0$ mode remains a bright mode. As we expect from the theory discussed in Sec. 3.3 all modes higher than the vacuum mode, i.e., $\frac{2m}{N} > 2d/\lambda$, are subradiant and have close to zero decay rate. In Fig. 3.4 (b) again the collective decay rate of the single ring configuration is plotted setting $d/\lambda = 0.5$. As all parameters of the system remain constant, we don't expect a change in the overall behaviour for both polarizations. However, the superradiant mode is at $m = \pm 2$ and the position of the light line is shifted to $\frac{2m}{N} = 2d/\lambda = 1$, resulting in the fact that there are no modes approaching $\Gamma_m/\Gamma_0 = 0$. Thus, there are no subradiant modes. This coincides with the theoretical prediction.

3.3.2 Collective Decay Rates and Energy Shifts as Function of System Parameters

First we analyze the collective behaviour depending on the dipole orientation for a ring of size $N = 9$. In Fig. 3.5 (a) we show the dependence of the collective energy shifts following Eq. (3.16)

[1]The dispersion relation of the ring configuration is defined via the real part of the eigenvalues. However, the real and imaginary part are tightly connected and provide the same information about the light-line. As we are more interested in the decay rate in subsequent chapters, we stick to plotting the collective decay rate and study the light line in this context.

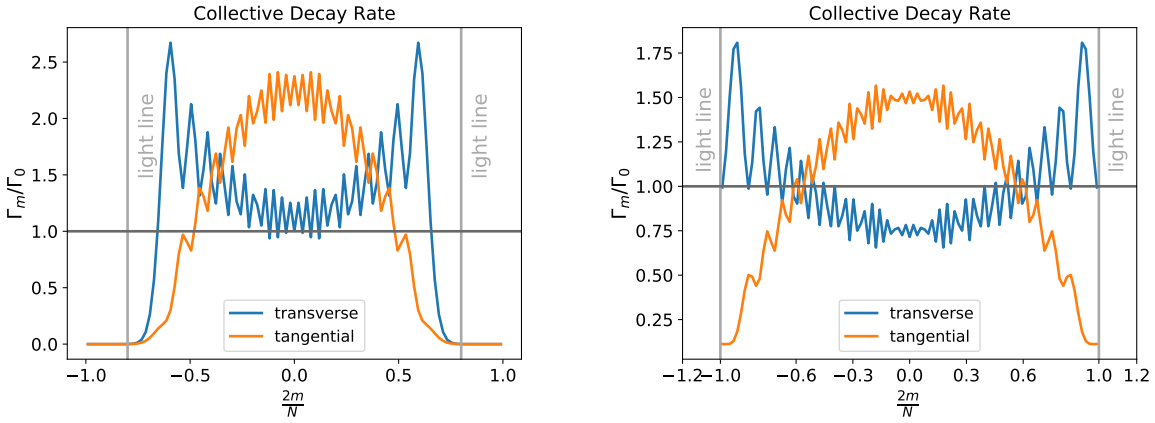

(a) (b)

Figure 3.4: *Collective decay rate for different modes* with angular momentum m *for* $N = 101$ *atoms in the ring.* **(a)** The inter-particle distance is $d/\lambda = 1/3$. According to Sec. 3.3 the light line is at $2m_{\text{ll}}/N = 0.6$ **(b)** The inter-particle distance is $d/\lambda = 1/2$. Thus, the light line is at $2m_{\text{ll}}/N = 1$.

depending on the dipole orientation represented by the azimuthal angle ϕ. Using spherical coordinates for the dipole vector, $\phi = 0$ refers to the case of transverse dipole orientation and $\phi = \frac{\pi}{2}$ to tangential polarization. At approximately $\phi = \frac{\pi}{6}$ there is an inversion in sign of J_m and the amplitude grows for an increasing angle ϕ. Summing up, the energy-shifts are smaller for transverse polarization and the amplitude increases significantly for tangential polarization with an inverse sign. Next, we have a closer look at the behaviour of the collective decay rate while varying the orientation of the dipoles from transverse to tangential plotted in Fig. 3.5 (b). The mode $m = 0$ is dominant, i.e., superradiant in the case of transverse polarization. The $m = \pm 1$ modes are radiant while the $m = \pm 2,\ \pm 3,\ \pm 4$ modes are subradiant. Rotating the dipole vector around the angle ϕ the decay rate of the $m = 0$ mode shrinks while the amplitude of the $m = \pm 1$ modes increase. In fact, for tangential polarization the $m = \pm 1$ modes are dominant. The highest modes, namely $m = \pm 3,\ \pm 4$ don't change there behaviour, i.e., they stay subradiant for every polarization while the decay rate of the $m = \pm 2$ modes increases a bit.
In Fig. 3.6 we split up the preceding plot into each mode m and plot the decay rate for different distances d/λ in order to get a better insight into the dynamics. For $d/\lambda = 0.1$ you obtain the same results we observed in Fig. 3.5. Apparently, transverse polarization provides the greatest effects regarding sub- and superradiance. The best superradiance is obtained at the $m = 0$ mode for $d/\lambda = 0.1$. In general, one can say that it is more favourable to work at small distances and small modes in order to obtain the most radiant states. However, for the modes $m = \pm 2,\ \pm 3,\ \pm 4$ you can increase the decay rate by increasing the inter-particle distance for all polarizations. On the other hand, rather small distances and higher modes provide subradiance. In particular, the $m = \pm N/2$ modes give rise to the best subradiance independent of the dipole orientation.

Varying the interaction strength between the atoms is of interest. In order to do this, we study the dependence of the collective phenomena on the inter-particle distance d. In Fig. 3.7 the collective decay rate Γ_m is plotted as a function of the inverse distance between the quantum emitters d in units of the transition wavelength λ (compare Eq. (2.16)). Here we compare the

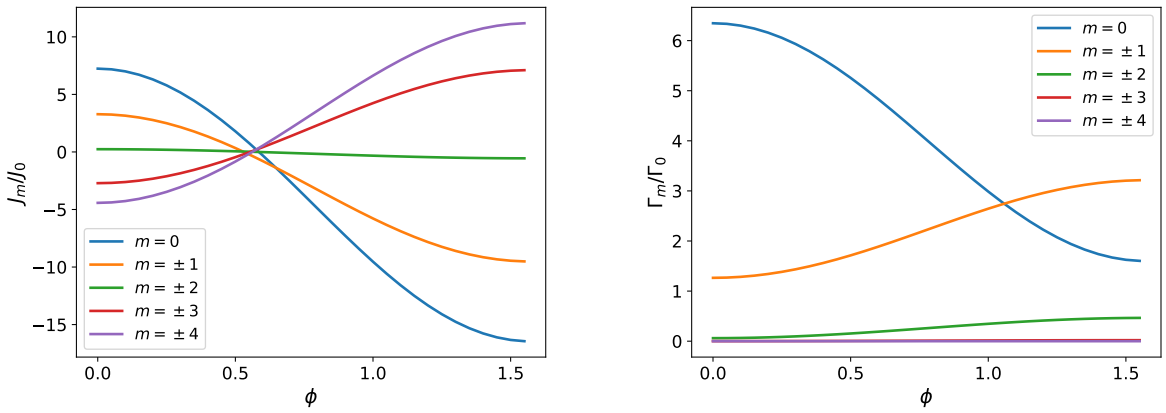

(a) (b)

Figure 3.5: *Collective energy shifts and decay rates of a single ring depending on the orientation of the dipoles for $N = 9$ atoms and $d/\lambda = 0.1$.* **(a)** The collective energy shift is plotted as a function of the azimuthal angle ϕ (given in radians). The mode $m = 0$ is dominant with respect to the amplitude of the shift and the $m = \pm 2$ modes have the smallest effective shift in energy. **(b)** The collective decay rate is plotted as a function of the azimuthal angle ϕ (given in radians). For transverse polarization one bright mode occurs at $m = 0$ whereas in the case of tangential polarization you have two superradiant modes at $m = \pm 1$.

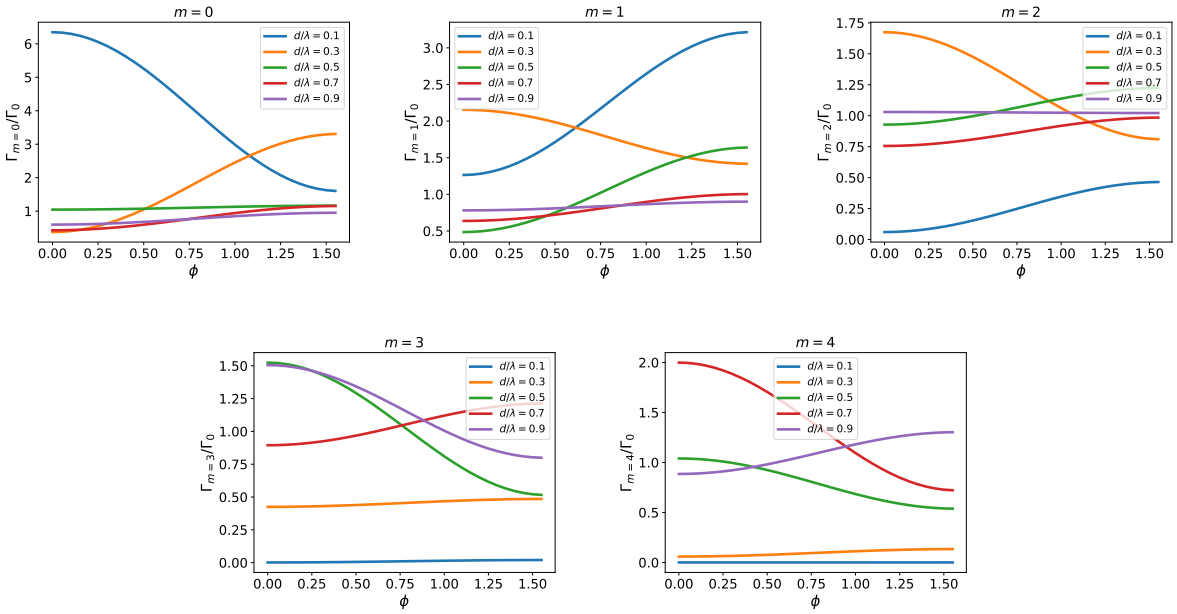

Figure 3.6: *Collective decay rates of the different angular momentum eigenmodes as function of the azimuthal angle ϕ (given in radians) enclosed by the atomic dipole and the normal of the ring plane for different m (plots) and inter-particle distances d (colors).* $\phi = 0$ corresponds to all dipoles arranged transversely while $\phi = \pi/2$ describes tangential dipoles.

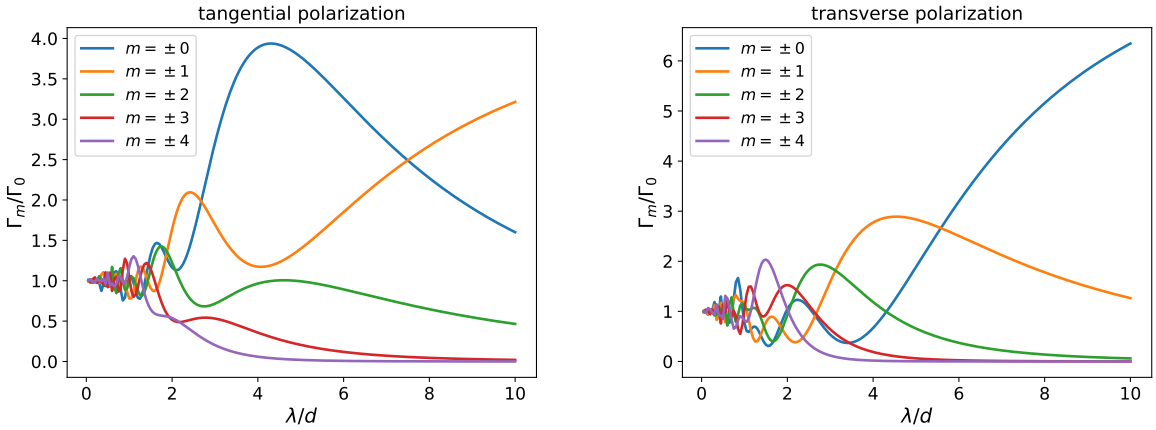

(a) (b)

Figure 3.7: *Collective decay rates depending on the inverse distance between the quantum emitters.* **(a)** Decay rates for different modes m for the dipoles oriented tangential to the plane of the ring with $N = 9$ emitters. In the Dicke limit two bright modes occur at $m = \pm 1$. **(b)** Decay rates for different modes m for the dipoles oriented transverse to the plane of the ring with $N = 9$ emitters. In the Dicke limit one bright mode occurs at $m = 0$.

behaviour for different modes m and different dipole polarizations. For tangential polarization, depicted in Fig. 3.7 (a), two superradiant modes arise at $m = \pm 1$ in the limit of $d \to 0$ (Dicke Limit [7]), where the range of interaction is infinite. The mode $m = 0$ becomes subradiant in this limit. For transverse dipole orientation you observe one bright mode at $m = 0$ and $N - 1 = 8$ subradiant modes in the Dicke limit, as it is illustrated in Fig. 3.7 (b). In the limit of an infinite distance between the emitters $d \to \infty$ the atoms effectively do not recognize each other. Consequently the decay rate reduces to the single atom decay rate Γ_0 for both polarizations.

In Fig. 3.8 the decay rate Γ_m is plotted for an increasing density of emitters in a ring of constant size $R/\lambda = 1/2$ for transverse and tangential polarization at different modes. For the superradiant mode - at $m = \pm 2$ for transverse and at $m = 0$ for tangential polarization - the decay rate scales linearly with N, i.e., $\Gamma_{\max} \propto N\Gamma_0$. The behaviour changes significantly when keeping the distance between the emitters constant while increasing the number of atoms N in the ring. In this case the most subradiant mode scales exponentially with N as depicted in Fig. 3.9 (a), where the scaling for tangential polarization is worse than for transverse. Thus, the lifetime τ_m of the state increases accordingly as $\Gamma_m = 1/\tau_m$. This is an important feature of a ring configuration. For tangential polarization the superradiant mode reaches its maximum at $N = 7$ atoms. Afterwards the amplitude decreases the more atoms you add to the ring. On the other hand the decay rate is increasing with N for transverse polarization, however mainly in the region of smaller N the superradiant decay rate is significantly smaller than for tangential polarization.
The covered energy-shift spectrum becomes larger as the density of the rings increases. Furthermore the polarization of the dipoles determines whether brighter or darker modes are higher in energy as you can gather from Fig. 3.10. For transverse polarization, i.e., Fig. 3.10 (a) bright modes are higher in energy whereas the dark modes get a negative energy-shift. For tangential polarization, depicted in Fig. 3.10 (b), it's the other way around and dark modes are higher in energy. This result continues to be valid, when the ring is defined via the inter-particle distance

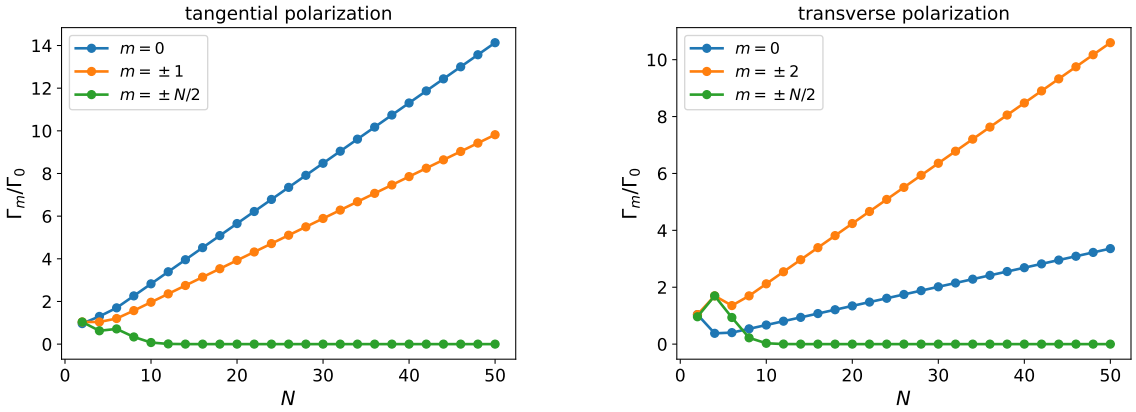

(a) (b)

Figure 3.8: *Collective decay rates depending on the number of atoms N in the ring.* **(a)** The radius is fixed to $R/\lambda = 1/2$ and the decay rate is plotted at different modes m for tangential dipole polarization. **(b)** As in (a), the radius is fixed to $R/\lambda = 1/2$ and the decay rate is plotted at different modes m, but for transverse dipole polarization.

d instead of the radius R.

3.4 Radiation Field Properties

In order to find the radiation pattern created by a given state of the ring, we compute the field intensity at a certain position $\vec{r}$ generated by the atoms at positions $\vec{r}_i$ and in that state, according to Eq. (2.17). Here we will study the field created by the single excitation collective eigenmodes of the ring, and thus, the expectation value in the fields expression is calculated with the eigenstates given in Eq. (3.18). The results are shown in Fig. 3.12 for transverse and in Fig. 3.11 for tangential polarization in the x y and in the x z-plane, respectively. As we have already discussed in Sec. 3.3, dark modes have a wave vector that is larger than the vacuum wave vector. Therefore the electromagnetic fields radiated transversely to the plane of the ring are suppressed and the light is guided along the ring. For instance this can be seen in Fig. 3.11 and Fig. 3.12 at the mode $m = 5$ in the x z-plane. In the x y-plane subradiant modes are characterized by a star-shaped pattern with a vanishing field in the center of the ring. Contrary to that, radiant and superradiant modes show a donut-shape. In case of the $m = 1$ mode for tangential polarization (cf. Fig. 3.11), the radiation is focused at the center of the ring as the dipoles acquire the right phase to maximally add constructively. In contrast, the radiation vanishes at the center of the ring for the $m = 0$ mode for which the dipoles do not acquire any additional phase. In this case, due to symmetry, all the dipole contributions exactly cancel leading to a vanishing field at the center. In the x z-plane the superradiant eigenstates are transversely oriented as for example in Fig. 3.11 (b) at the $m = 0$ mode.

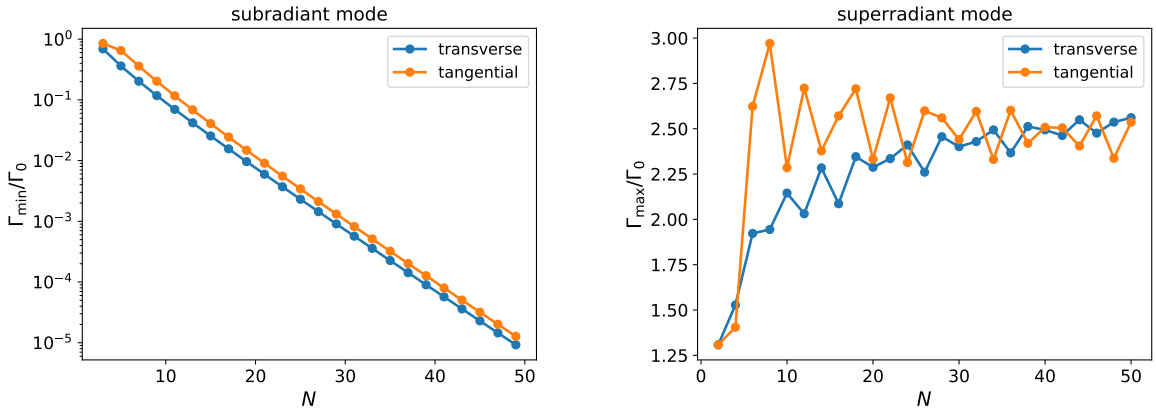

(a) (b)

Figure 3.9: *Most sub- and superradiant collective decay rate depending on the number of atoms in the ring for fixed inter-particle distance $d/\lambda = 1/3$ comparing transverse (blue) and tangential (orange) polarization.*

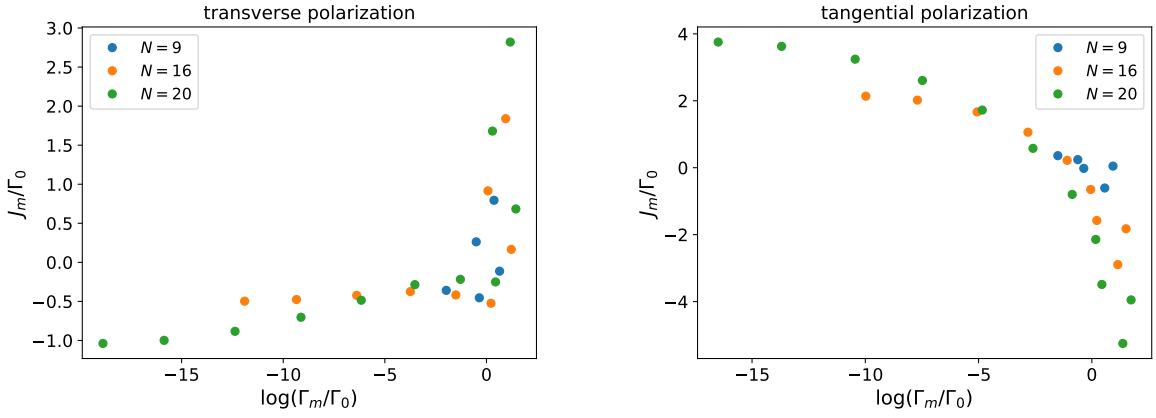

(a) (b)

Figure 3.10: *Collective energy-shifts plotted as a function of the collective decay rates.* We study the behaviour for both polarizations and for different number of atoms in a ring of constant size, i.e., $R/\lambda = 1/2$, implying that the ring becomes denser for increasing N.

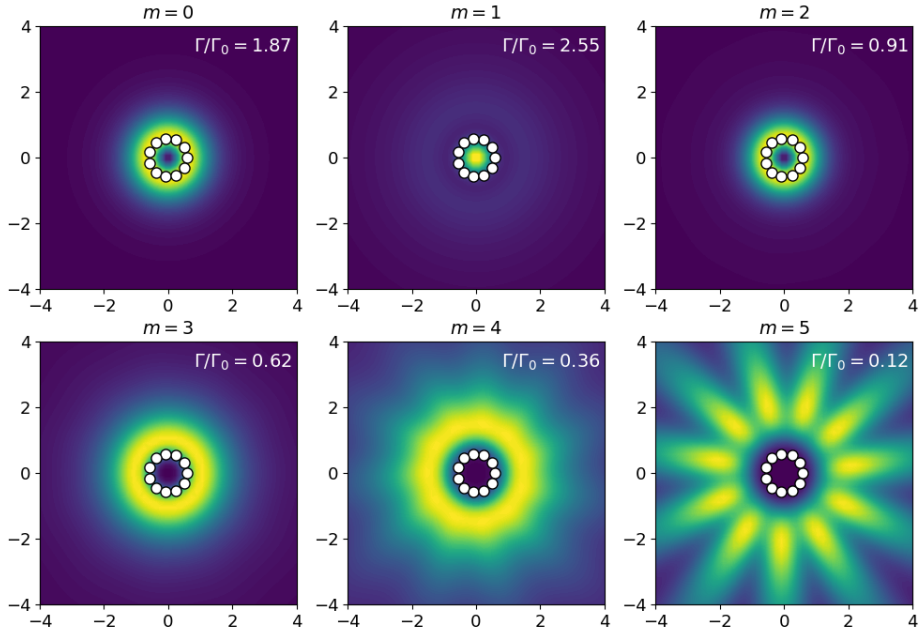

(a) x y-plane

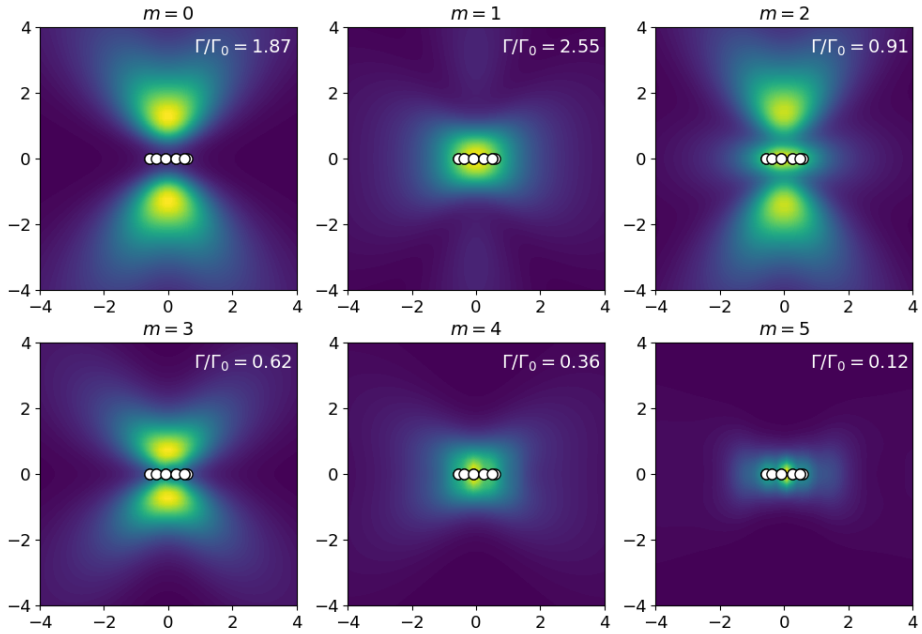

(b) x z-plane

Figure 3.11: *Radiation pattern of a single ring with* $N = 11$ *for tangential polarization.* The distance between the atoms is $d = 1/3$ and the observer is $d_{\text{obs}} = 2R$ above the respective plane. The intensity is normalized to its maximum.

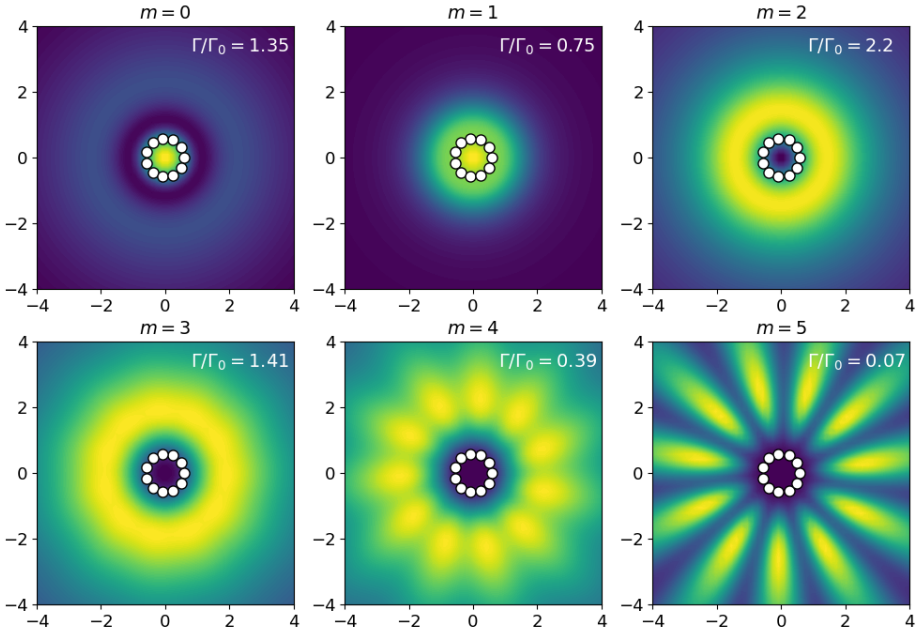

(a) x y-plane

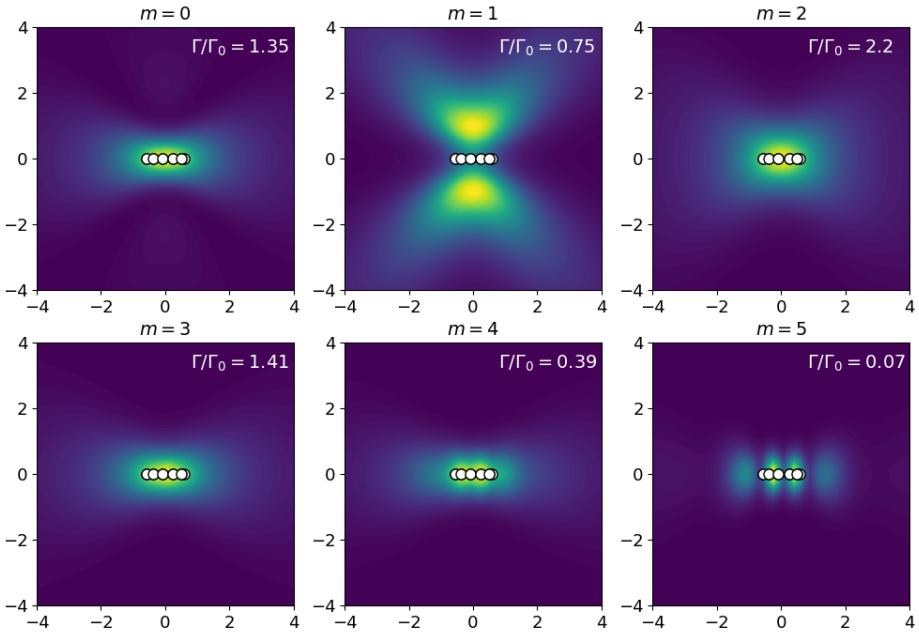

(b) x z-plane

Figure 3.12: *Radiation field pattern of a single ring with $N = 11$ for transverse polarization.* The distance between the atoms $d = 1/3$ and the observer is $d_{\text{obs}} = 2R$ above the respective plane.

Chapter 4

Two Coupled Identical Nano-Ring Structures

After the above review of the central radiative properties of single nano-rings we will now enter new physical territory and analyze the characteristics of two coupled identical nano-rings. As the system still keeps its angular symmetry, we can use a similar mathematical approach as in Chapter 3. Our first goal is thus to find an Ansatz to diagonalize the Hamiltonian analytically. As a first step we use a straightforward form of the above solution, which should be valid in case of identical rings. Due to symmetry we can expect that symmetric and anti-symmetric superpositions of the single ring eigenmodes correspond to collective modes of two identical coupled rings. In systems of unequal rings our Ansatz breaks down. As we see in the subsequent chapter, a more general Ansatz can be chosen in order to investigate radiation properties of more general double ring configurations with well defined angular symmetry. This discussion could be relevant in the context of light-harvesting complexes.

4.1 Analytical Diagonalization of the Effective Hamiltonian

As in the case of a single ring, the effective non-hermitian Hamiltonian can be written as

$$H_{\text{eff}} = \sum_{i,j=1}^{2N} \left[J_{ij} - i\frac{\Gamma_{ij}}{2} \right] \sigma_i^+ \sigma_j^- = \sum_{i,j=1}^{2N} G_{ij} \sigma_i^+ \sigma_j^- \tag{4.1}$$

with $G_{ij} = J_{ij} - i\frac{\Gamma_{ij}}{2}$. Now the indices $i, j = 1, \cdots 2N$ run over all lattice sites of the two rings. We label the lattice sites of the first (second) ring as $1, \cdots, N$ $(N+1, \cdots, 2N)$. Using a Spin-wave Ansatz, we are again able to analytically diagonalize it. We assume that we have a linear, two element, chain that is characterized by the linear momentum k_z and the distance z between the elements, each consisting of a ring itself. Therefore we take the same Ansatz as before and enlarge it by an additional exponential function. The Fourier transformed jump operators are then given by

$$\tilde{\sigma}_{m,k_z}^- = \frac{1}{\sqrt{2N}} \sum_j \mathrm{e}^{im\phi_j} \mathrm{e}^{ik_z d_j} \sigma_j^- \tag{4.2}$$

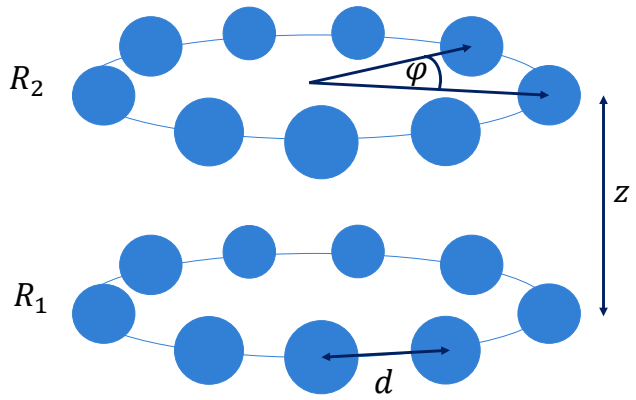

Figure 4.1: *Double ring configuration.*

with $k_z \in \{0, \frac{\pi}{z}\}$, $d_j \in \{0, z\}$ and $m = 0, \pm1, \pm2, \cdots, \lceil \pm(N-1)/2 \rceil$, where $\lceil \cdot \rceil$ is the ceiling function. Inserting this Ansatz into the effective Hamiltonian, we arrive at

$$H_{\text{eff}} = \frac{1}{2N} \sum_{ij} G_{ij} \sum_{m,m',k_z,k_z'} \mathrm{e}^{im\phi_i} \mathrm{e}^{-im'\phi_j} \mathrm{e}^{ik_z d_i} \mathrm{e}^{-ik_z' d_j} \tilde{\sigma}^+_{m,k_z} \tilde{\sigma}^-_{m',k_z'}. \tag{4.3}$$

As we already cared about the exponentials including the angular momentum m and the angles ϕ_j in Sec. 3.2, it remains to be checked whether the terms for $k_z \neq k_z'$ are vanishing in order to arrive at a diagonal Hamiltonian. Thus, we have to have a closer look at the sum

$$\sum_{k_z \neq k_z'} \mathrm{e}^{ik_z d_i - ik_z' d_j} = \mathrm{e}^{-i\pi d_j/z} + \mathrm{e}^{i\pi d_i/z}. \tag{4.4}$$

One can now make use of the rotational symmetry in the ring structure and it turns out that

$$\begin{aligned} i,j \in \mathrm{R}_1, \mathrm{R}_1: &\quad \mathrm{e}^{-i\pi 0/z} + \mathrm{e}^{i\pi 0/z} = 2 \\ i,j \in \mathrm{R}_2, \mathrm{R}_2: &\quad \mathrm{e}^{-i\pi z/z} + \mathrm{e}^{i\pi z/z} = -2 \\ i,j \in \mathrm{R}_1, \mathrm{R}_2: &\quad \mathrm{e}^{-i\pi 0/z} + \mathrm{e}^{i\pi z/z} = 0 \\ i,j \in \mathrm{R}_2, \mathrm{R}_1: &\quad \mathrm{e}^{-i\pi 0/z} + \mathrm{e}^{i\pi z/z} = 0. \end{aligned} \tag{4.5}$$

Consequently all terms for $k_z \neq k_z'$ drop out. We are left with an expression that depends on m and k_z and with a diagonal Hamiltonian

$$H^{\text{diag}}_{\text{eff}} = \sum_{m,k_z} G_{m,k_z} \tilde{\sigma}^+_{m,k_z} \tilde{\sigma}^-_{m,k_z} = \sum_{m,k_z} \lambda_{m,k_z} \tilde{\sigma}^+_{m,k_z} \tilde{\sigma}^-_{m,k_z}, \tag{4.6}$$

respectively. The eigenvalues λ_{m,k_z} are then given by

$$\lambda_{m,k_z} = \frac{1}{2N} \sum_{i,j} \mathrm{e}^{im(\phi_i - \phi_j)} \mathrm{e}^{ik_z(d_i - d_j)} G_{ij} \tag{4.7}$$

The eigenstates are accordingly a symmetric or anti-symmetric superposition of the single ring eigenstates, i.e.,

$$|\Psi_{m,\alpha}\rangle = \frac{1}{\sqrt{2N}} \sum_{j=1}^{N} \mathrm{e}^{-im\phi_j} \{\sigma_j^+ + (-1)^\alpha \, \sigma_{j+N}^+\} \, |g\rangle^{\otimes 2N}, \tag{4.8}$$

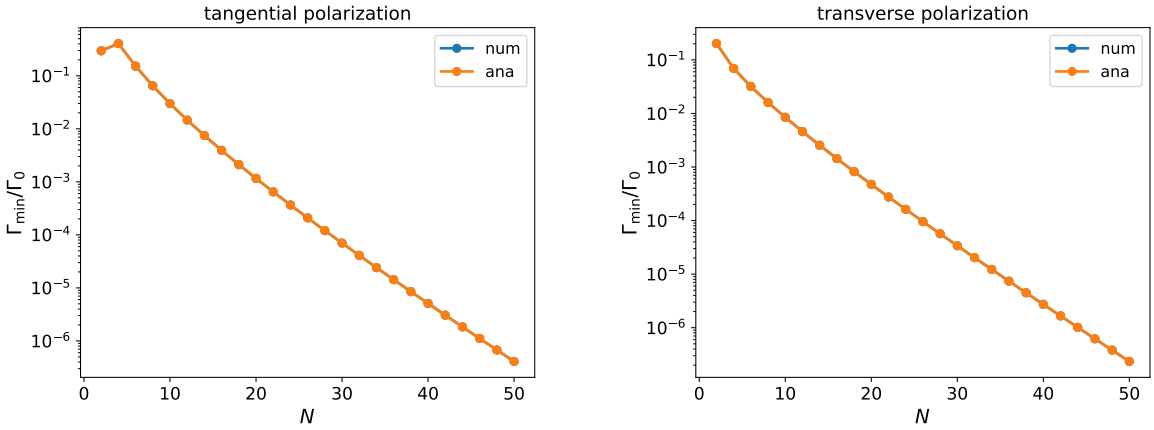

(a) (b)

Figure 4.2: *Numerical and analytical decay rate of the most subradiant eigenmode for two identical rings,* $\Gamma_{\min}$ *as a function of the number of atoms of one ring* N. The results are shown for **(a)** tangential and **(b)** transverse dipole orientation with distances $d/\lambda = 1/3$ and $z/\lambda = 1/3$. In both cases the exponential behaviour is salient and the scaling is of the same order. The results agree perfectly within the plot resolution.

where $\alpha = 0$ corresponds to the symmetric and $\alpha = 1$ to the anti-symmetric case. As in the single ring case one can now have a look at the collective decay rates

$$\Gamma_{m,\alpha} = -2\ \Im(\lambda_{m,\alpha}) \tag{4.9}$$

and the collective energy-shifts

$$J_{m,\alpha} = \Re(\lambda_{m,\alpha}). \tag{4.10}$$

4.2 Validity of the Symmetric and Anti-Symmetric Spin-Wave Superposition

In this section we will have a look at the validity of our model in case of two identical and two distinct rings. Comparing the numerical and analytical results, we are able to extract this information. The most subradiant mode is defined via $\min\left(\Gamma_{m,\alpha}\right)$ whereas the superradiant mode is given by $\max\left(\Gamma_{m,\alpha}\right)$. Using the frameworks QuantumOptics and CollectiveSpins in Julia [20] the corresponding numerical results for the decay rates are calculated.

4.2.1 Validity of the Ansatz for Coupled Identical Rings

We denote rings as identical, if both rings have the same dipole orientation, i.e., $\vec{\mu}_j = \vec{\mu}_{j+N}$ with $j \in [1, N]$ for tangential and $\vec{\mu}_j = \vec{\mu}_i$ with $j, i = [1, 2N]$ for transverse polarization. The same absolute value is still required. Further, we expect equal inter-particle distances in R_1 and R_2, as shown in Fig. 4.2.
First, we study the dependence of the subradiant decay rate on the number of atoms N for a fixed inter-particle distance d since we found a characteristic, exponential behaviour in the single ring

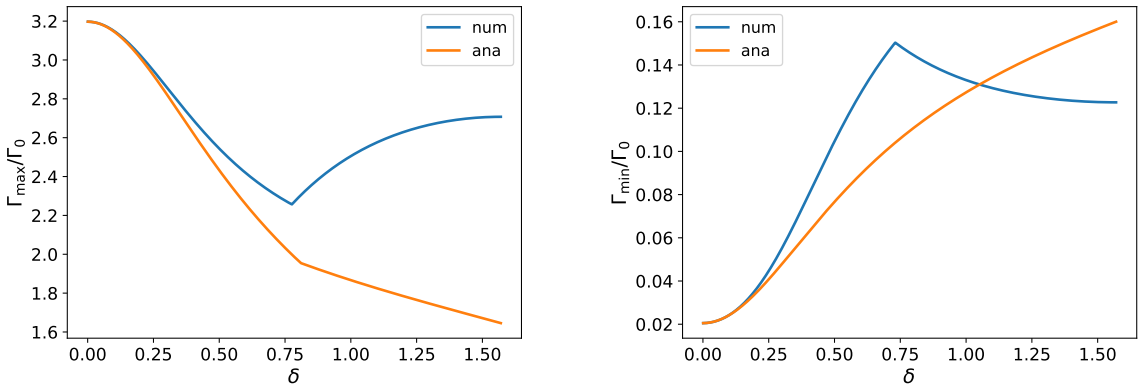

(a) (b)

Figure 4.3: *Most radiant* **(a)** *and subradiant* **(b)** *decay rate obtained by numerical and analytical evaluation, depending on the azimuthal angle δ of the dipole orientation of the upper ring atoms (given in radians).* The polarization of the lower ring is transverse, whereas the one of the upper ring is varied from $\delta = 0$ (transverse) to $\delta = \pi/2$ (tangential). The parameters of the system are $d/\lambda = z/\lambda = 1/3$. One finds good agreement in a small range around the polarization of the lower ring.

case. In Fig. 4.2 we plotted the subradiant modes for tangential and transverse dipole orientation as a function of N for parameters $z/\lambda = d/\lambda = 1/3$. The analytical and numerical decay rates coincide perfectly in both plots within the plot resolution. Furthermore, the same exponential behaviour is found as for a single ring configuration. The agreement of numerical and analytical results is supported by studies of the variation of any other system parameter. Thus, the analytical Ansatz provides the correct solutions and the spin-wave Ansatz is applicable for two identical rings. In the next section we will mainly use the numerical results keeping in mind that the analytical Ansatz yields to the same outcome.

4.2.2 Breakdown of the Ansatz for Unequal Coupled Rings

Here we generalize to double-ring configurations where one or more parameters, as for example the relative dipole orientation or the inter-particle distance differ between the two rings. Within one ring we assume to have rotation symmetry for particles.

As a first example we consider the lower ring made up of two-level emitters with transverse dipole orientation, whereas the upper ring emitters polarization has a tangential and a varying z-component. We express the dipole vector $\vec{\mu}_{j+N}$ for $j \in [1, N]$ in spherical coordinates and increase the azimuthal angle from $\delta = 0$ (transverse) to $\delta = \pi/2$ (tangential). The analytical and numerical results of the maximum and minimum decay rates for this case are shown in Fig. 4.3. For the maximal decay rate, depicted in Fig. 4.3 (a), the analytical result coincides with the numerical one until approximately $\delta = 0.25$ rad $\approx 14.3°$. The larger the deviation from the orientation of the lower ring, the bigger the error of our analytical model. A similar conclusion is obtained for the subradiant mode. Here the range of agreement is not as large as with the superradiant mode. A second example is depicted in Fig. 4.4. We fix the position vector of the lower ring R_1 and add

an additional rotation of angle θ in the position vector of the upper ring R_2, i.e.,

$$\vec{r}_j^{\,R_1} = \begin{bmatrix} R\ \cos(\phi(j)) \\ R\ \sin(\phi(j)) \\ 0 \end{bmatrix}, \quad \vec{r}_j^{\,R_2} = \begin{bmatrix} R\ \cos(\phi(j)+\theta) \\ R\ \sin(\phi(j)+\theta) \\ z \end{bmatrix}. \tag{4.11}$$

Rotating the upper ring from $\theta = -\Delta\phi/2 = \pi/9$ to $\theta = \Delta\phi/2 = \pi/9$ the behaviour of the decay rates and, in particular, the agreement of numerical and analytical results is strongly dependent on the dipole orientation and the mode. For tangential polarization the decay rates at the superradiant mode arising from numerical and analytical calculations coincide perfectly as it is depicted in Fig. 4.4 (a). A whole different situation is presented in Fig. 4.4 (b). Here we plot the superradiant decay rate for transverse polarization. The results obviously deviate, even though the effective deviation is rather small.
We conclude that our model is not reliably applicable in the case of two distinct rings. However, in some configurations, as in Fig. 4.4(a), and in small ranges around the identical case, as in Fig. 4.3 (b), the results show a good agreement. This can be traced back to the fact, that the most important step in our diagonalization consists in the rotational symmetry of the single and double ring configuration that allows us to transform our Hamiltonian analytically to its diagonal form. It has to be assumed that this symmetry is in general broken as soon as you change one parameter of only one subsystem. Some alignments maintain this symmetry, however this has to be checked for every individual configuration.

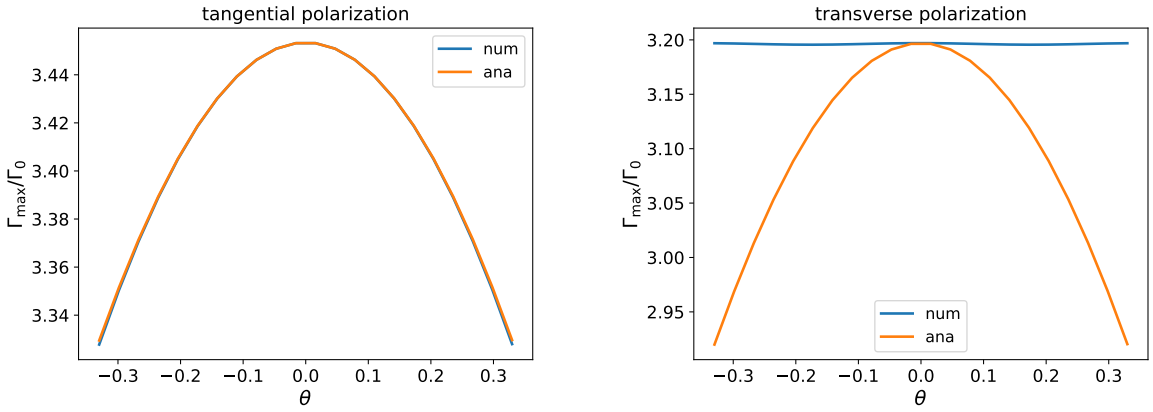

(a) (b)

Figure 4.4: *Superradiant decay rates obtained from numerical and analytical evaluation for tangential* **(a)** *and transverse* **(b)** *polarizations, depending on the additional rotation angle θ (in radians) of the upper ring.* The system parameters are $d/\lambda = z/\lambda = 1/3$. Both rings consist of $N = 9$ identical quantum emitters. It can be seen that the numerical and analytical results do not coincide for transverse polarization.

4.3 Optical Properties of Two Coupled Identical Rings

The simplified spin-wave Ansatz is applicable in the case of identical rings and we study the properties for this configuration in more detail in the following section.

4.3.1 Collective Decay Rates

First we want to study the collective decay rates for different angular momenta m and compare it to the results of the single ring configuration. The result is shown in Fig. 4.5. Here we plot the decay rate as a function of the angular momentum m[1] for $N_{\mathrm{tot}} = 202$ atoms. Contrary to the single ring case one has to take care of an additional degree of freedom, the linear momentum k_z. As a consequence, the dispersion relation shows two bands, that arise from the symmetric and anti-symmetric superposition of the single ring eigenstates, as shown in Fig. 4.5. The symmetric case shows a similar behaviour as the decay rate of a single ring for both polarizations discussed in Sec. 3.3.1. The superradiant modes are at the edge of the non-guided region whereas the subradiant modes are found beyond the light line, i.e., in the guided region (Sec. 3.3) for transverse dipole orientation (cf. Fig. 4.5 (a) and (c)). The $m = 0$ mode is radiant. In the case of tangential polarization (cf. Fig. 4.5 (b) and (d))) the superradiant modes are centered around the $m = 0$ mode for a symmetric superposition of the eigenstates. Having a look at the anti-symmetric superposition, the $m = 0$ mode is superradiant. The maximal decay rate is much smaller than in the transverse case for both, symmetric and anti-symmetric superpositions. Also in the guided mode region, the decay rate in the anti-symmetric case is approximately one magnitude lower than in the symmetric case. The decay rate for an anti-symmetric superposition doesn't show as distinct oscillations as for a symmetric superposition. This could be led back to the fact, that in the symmetric case the radiation, and therefore, going hand in hand with this, interference effects are much stronger than in the anti-symmetric case.

The determination of the light line in the double ring case is interesting, indeed. For a single ring we have seen that the light line - the boundary between radiant and subradiant states - is close to[2] $\frac{m}{N} = d/\lambda$. We find that this value also corresponds to the light line for the two rings case. Thus, as shown in Fig. 4.5, one concludes that it is possible to broaden or narrow the radiant area by increasing and decreasing, respectively, the distance between the atoms in one ring with respect to the light wavelength. Whereas in Fig. 4.5 (a) and (b) the inter-particle distance is set to $d/\lambda = 1/3$, in Fig. 4.5 (c) and (d) we decrease the distance to $d/\lambda = 0.1$ while keeping the inter-ring distance constant at $z/\lambda = 1/3$. It is evident that the light line is shifted to smaller values of m.

In order to check the influence of the z component (separation between the two rings) on the light line position, we study the collective decay rates and shifts while changing the z-parameter. Varying z/λ the overall behaviour remains the same, however, in the symmetric case, plotted in Fig. 4.6 (a), the decay rate decreases for higher distances between the rings. In contrast to that, in the anti-symmetric case, illustrated in Fig. 4.6 (b), the decay rate increases with increasing gap-size between the rings. As z gets larger, the two rings become decoupled, and both cases approach the single ring case the symmetric approaches from above whereas the anti-symmetric approaches from below. For a smaller value of z, the result can be understood via the formation of dimers consisting of two atoms, one of each ring. In the symmetric case, the dimers are bright (in a symmetric superposition) and increase the decay rate, whereas in the anti-symmetric case they are dark (in an antisymmetric superposition).

The coupling between the two rings can in principle influence the position of the light line.

[1] In the limit of infinitely many rings above each other, one would obtain a 2D dispersion relation since k_z would be continuous. As we only deal with two rings, we study the light line for the symmetric and anti-symmetric case separately.

[2] As mentioned in Sec. 3.3, the position of the light line is exact in the limit of an infinite chain, i.e., a ring with radius $R \to \infty$.

For a large value of the interring distance z, the size of the light cone does not seem to change significantly, as shown in Fig.4.6 (b). In the limit of $z \to \infty$, both cases, symmetric and antisymmetric should provide the same results. This is confirmed by our studies. It seems like the light line is shifted towards the expected value for $z \to \infty$ (cf. Fig. 4.6 (a)). However, in the limit of $z \to 0$, the light line is slightly shifted towards smaller values of m/N (thus increasing the guided mode region) for the antisymmetric band, as shown in Fig. 4.6 (b).

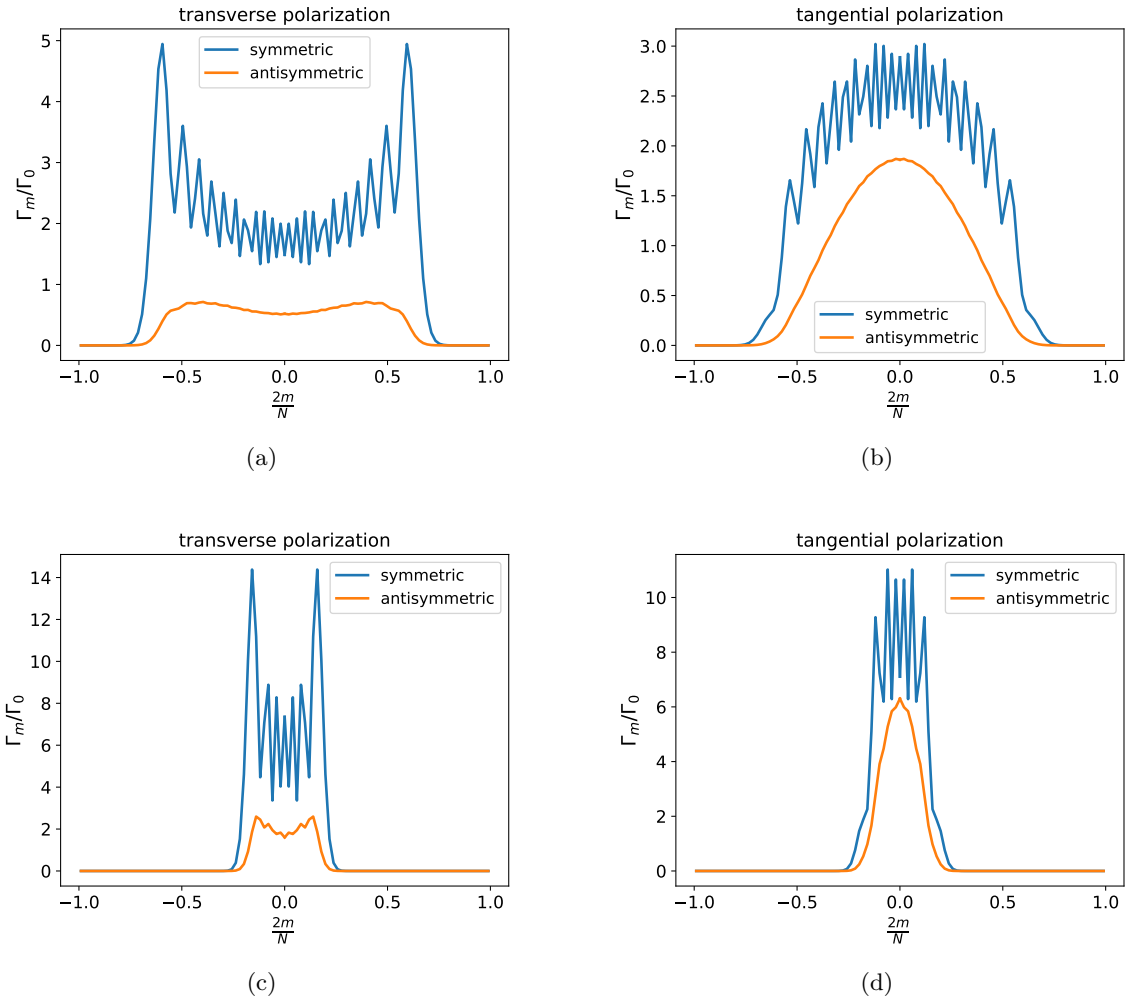

Figure 4.5: *Collective decay rate of a double ring configuration as a function of the angular momentum m of the eigenmodes.* The decay rate Γ_m of the symmetric (blue) as well as the anti-symmetric (orange) cases are plotted for different values of m (normalized by a factor N, for $2N = 202$ atoms). The parameters of the rings are: **(a)** $d/\lambda = z/\lambda = 1/3$, and transverse dipole orientation; **(b)** $d/\lambda = z/\lambda = 1/3$, and tangential dipole orientation; **(c)** $d/\lambda = 0.1$, $z/\lambda = 1/3$, and transverse dipole orientation; **(d)** $d/\lambda = 0.1$, $z/\lambda = 1/3$ and tangential dipole orientation. The symmetric case shows a similar behaviour than the dispersion relation of a single ring. The code for these plots is presented exemplary in Appendix A.

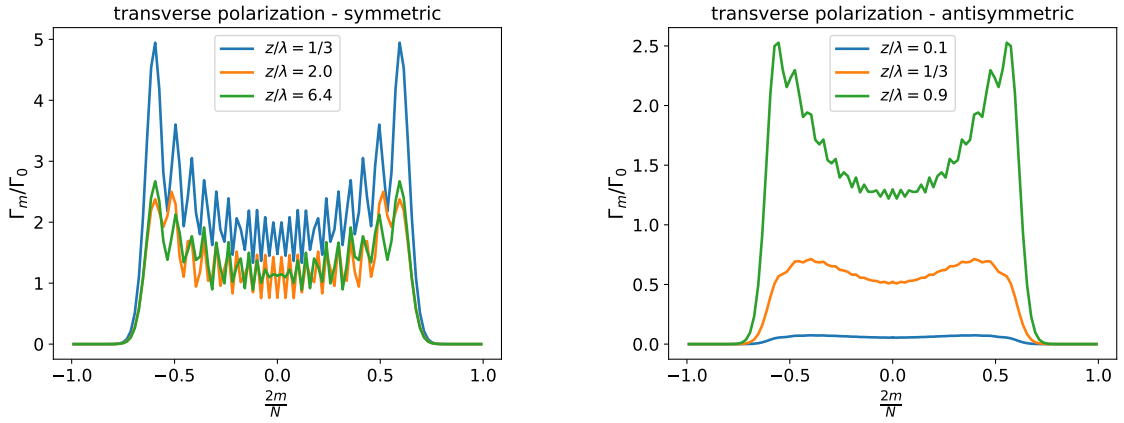

(a) (b)

Figure 4.6: *Collective decay rate of an identical double ring configuration as a function of the angular momentum m of the eigenmodes, for different vertical inter-ring distances.* The collective decay rates for transverse polarization and an inter-particle distance $d/\lambda = 1/3$ is plotted in the **(a)** symmetric and in the **(b)** anti-symmetric case for three different values of z/λ in order to study the position of the light-line depending on the distance between the rings.

4.3.2 Scaling of the Optimal Subradiant Mode in Double Rings

The special exponential suppression of the decay rate of the most subradiant mode is not only observable in the single ring case, but it is also present in a double ring configuration. The aim of this section is to find configurations that suppress further the decay rate of the subradiant modes, for a fixed number of quantum emitters. Furthermore, we want to figure out whether it is more favourable to arrange N atoms in a single ring or form two double rings with $N/2$ atoms each.

Varying the parameters z and d, the scaling with N of the most subradiant decay rate can be modified. In general, we aim for a steeper and lower exponential behaviour when doing a log-plot for a varying number of atoms in one ring. In Fig. 4.7 (a) we fix the distance between the two rings to $z/\lambda = 1/3$ and show the exponential decay of the decay rate for four different inter-particle distances d/λ. Now, picking the case of $d/\lambda = 0.3$, we try to improve the scaling in Fig. 4.7 (b) by varying the inter-ring distances z/λ. The smallest z/λ value that provides us the best scaling is $z/\lambda = 0.009$. Here we reach values below $\Gamma_{\text{min}}/\Gamma_0 = 10^{-9}$ for $N_{\text{tot}} = 100$ atoms in the system. This behaviour even beats the scaling of a single ring as it is shown in Fig. 4.7 (c). Here we picked the same inter-particle distances in the single and double ring case. In order to compare both cases, we plot the decay rates as a function of the total number of atoms N_{tot} in a single ring and in the double ring, respectively. For $N_{\text{tot}} < 90$ it is more favourable to arrange the atoms in a double ring configuration than in a single ring. In this case again two nearest sites, one from the lower and one from the upper ring, form an anti-symmetric dark or symmetric bright dimer which reduces or enhances the overall decay rate. When you want to have more atoms in the system, it is more efficient to go back to a single ring. In this case the smaller curvature of the single ring (with more atoms) compensates and leads to a smaller decay. This threshold value of N might change with the inter-particle distance d.

One of the most important features of a double ring compared to a single ring can be seen

in Fig. 4.7 (d). Before, we discussed which configuration is favourable for arranging N_{tot} atoms - either in a single or double ring - in order to achieve the best scaling. We see, that we are able to find geometries that lead to an improvement of the scaling of a double ring compared to the single ring (cf. Fig. 4.7 (c)). As already discussed in the previous section, the double ring is able to build dark dimers that decrease the minimal decay rate even more for $z/\lambda < d/\lambda$. Thus we expect, that the double ring decay rate beats the single ring decay rate for an equal inter-particle distance d having N atoms arranged in a single ring and $2N$ atoms in a double ring in this regime. In the regime, where $z/\lambda \leq d/\lambda$, each ring of the double ring can be seen as dipole itself. These dipoles can form again an anti-symmetric superposition decreasing the subradiant decay rate. This case is depicted in Fig. 4.7 (d) for $d/\lambda = z/\lambda = 1/3$ and our expectations are verified. For $z/\lambda \gg d/\lambda$ the rings are decoupled and you approach the single ring decay rate.

4.3.3 Further Characteristics of Double Rings

In the following section we want to study more special characteristics of a double ring configuration. In Fig. 4.8 we have a closer look at the superradiant mode of the double ring for transverse polarization. In Fig. 4.8 (a) plotting the most superradiant mode $\Gamma_{\max}/\Gamma_0$ as a function of the number of atoms for transverse dipole orientation, we compare the analytical with the numerical results assuring ourselves that our Ansatz remains applicable. As they have a perfect overlap within the plot resolution we conclude, that our Ansatz is indeed adequate for the superradiant mode. The overall behaviour in this plot is similar to the one of the single ring.

Therefore we study the N-dependence in more detail via the contour plot, that you can see in Fig. 4.8 (b). Here the superradiant mode is plotted for different values of N and z/λ. The closer the rings are and the smaller z/λ is, respectively, the higher the maximal decay rate $\Gamma_{\max}/\Gamma_0$. This maximal value can be increased on the other hand by increasing the number of atoms N in the rings which leads to an effective pairing of atoms j and $j+N$ for $j \in [1, N]$ as we keep our inter-particle distance d constant. However, you can't identify a specific behaviour or periodicity. For tangential dipole orientation we come to the same conclusion although the behaviour is different. In Fig. 4.9 (a) the maximum decay rate becomes apparent at $N = 7$ atoms which coincides with the observation in the single ring case. Increasing the number of atoms even further the maximum decay rate decreases. However our analytical Ansatz is appropriate. As we did before, we now have a closer look at the superradiant decay rate in a contour plot in which we vary both, the number of atoms N and the inter-ring distance z. Decreasing the distance between the rings you reach shorter lifetimes of the states. However, opposite to the case of transverse polarization, we see that increasing the number of atoms in one ring, the maximal decay rate decreases which is counter-intuitive. The maximum possible value of $\Gamma_{\max}/\Gamma_0$ we obtain by arranging $N = 7$ atoms at very small inter-ring distances. Furthermore we can identify an extra region, between $z/\lambda = 0.5$ and $z/\lambda = 0.9$, in which the decay rate increases again. There is evidence to suggest that there is kind of a periodicity in this behaviour.
In summary, for transverse polarization it's more favourable to arrange a large number of atoms in rings that are close to each other in order to reach the best superradiance. On the other hand, for tangential polarization it's better to keep the number of atoms and the inter-ring distance small.

Having discussed the dependence of the decay rates on the number of atoms in a double ring, we want to study the dependence of the decay rates on the inter-ring and inter-particle distance, respectively.
In Fig. 4.10 (a) we plot the decay rate at the most subradiant mode of the double ring for a varying

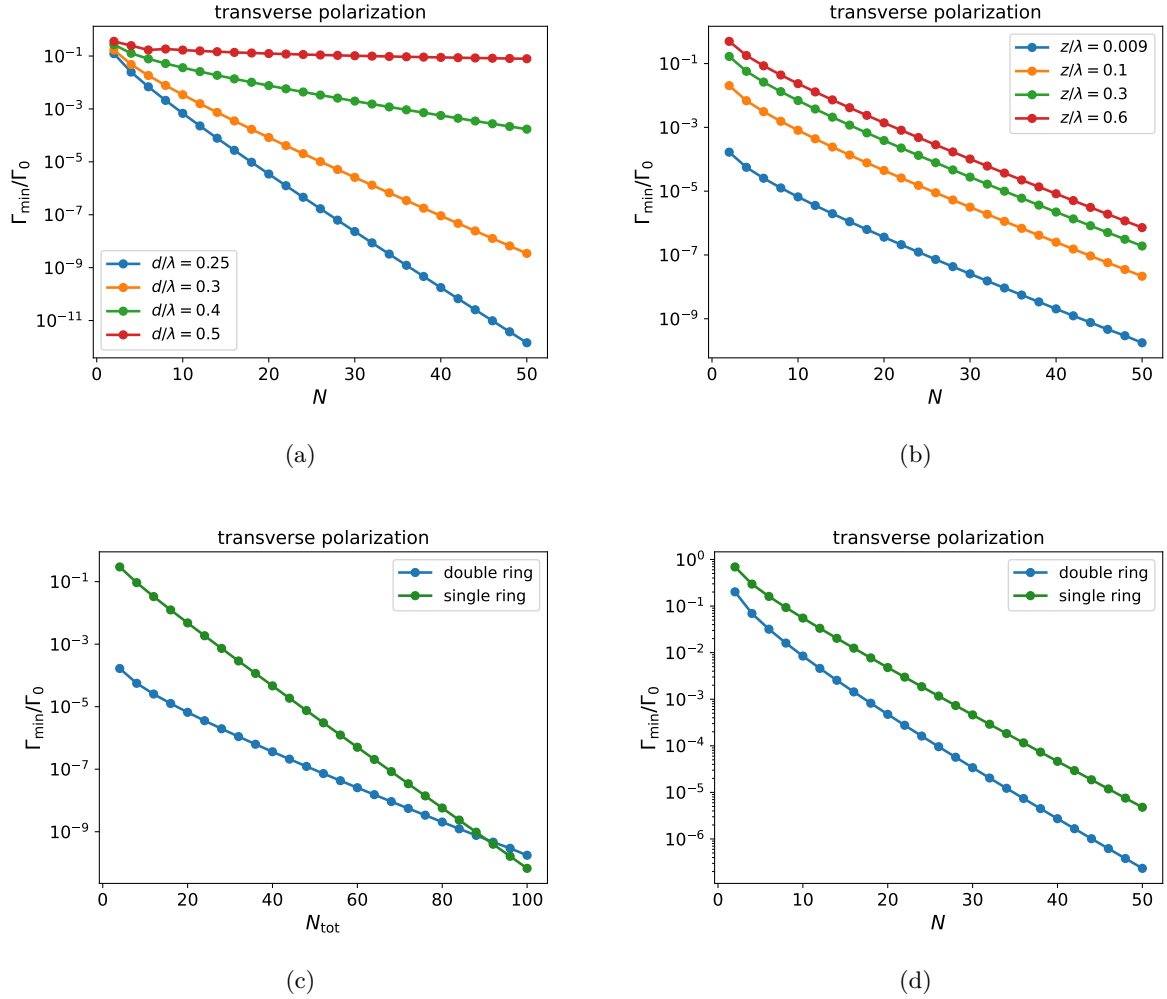

Figure 4.7: *Improvement of the scaling of the most subradiant mode decay* $\Gamma_{\min}$ *with atom number.* The decay rate of the most subradiant mode is plotted for transverse polarization as a function of the number of atoms N in one ring. **(a)** The inter-ring distance is fixed to $z/\lambda = 1/3$ and the decay rate is plotted for different values of d. **(b)** The inter-particle distance is fixed to $d/\lambda = 1/3$ and the decay rate is plotted for different values of z/λ. **(c)** Picking the distances that lead to the best scaling, i.e., $d/\lambda = 1/3$ and $z/\lambda = 0.009$, the double ring decay rate is compared to the single ring decay rate, for transverse polarization. N_{tot} corresponds to the total number of atoms in the double ring configuration or in the single ring. **(d)** Comparison between the double ring and single ring most subradiant decay rates, as a function of N atoms in each of the rings. The atoms are transversely polarized and have an inter-particle distance $d/\lambda = 1/3$. The inter-ring distance in the double ring is chosen to be $z/\lambda = 1/3$.

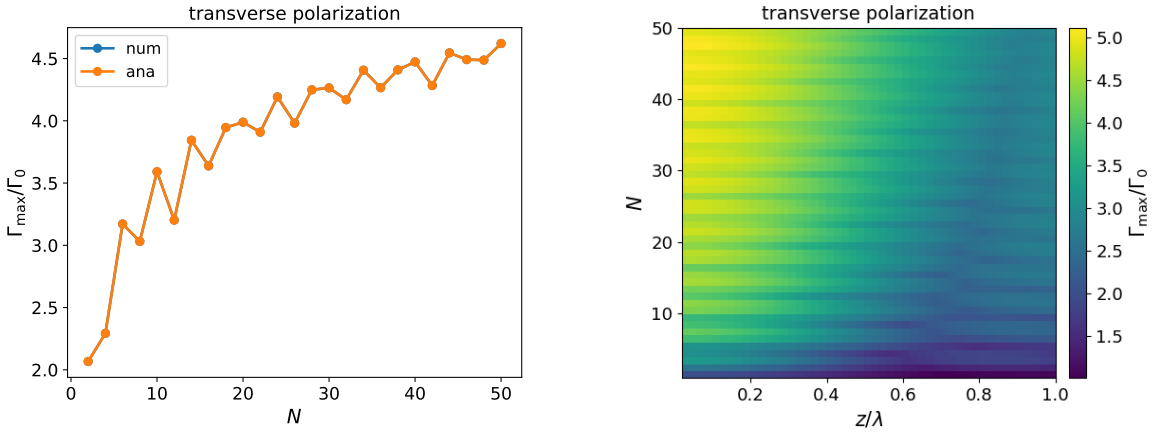

(a) (b)

Figure 4.8: *Most superradiant decay rate depending on number of atoms in one ring N and the distance between two rings z/λ for transverse dipole orientation and inter-particle distance $d/\lambda = 1/3$.* **(a)** The inter-ring distance is $z/\lambda = 1/3$ and the results arise from analytical and numerical calculations. **(b)** The maximal decay rate is plotted as a function of the number of atoms N and the distance between the rings z/λ in a contour plot.

distance between the two rings z/λ for $d/\lambda = 1/3$ and $N = 9$ atoms on a logarithmic scale. The smaller the distance z/λ, the smaller values you reach for the decay rate. This can be led back to the formation of dark dimers for small z that reduce the decay rate even further. On the other hand, you cannot increase the subradiant mode to infinity when increasing the distance between the rings as you expect. In actual fact you approach a maximum value that coincides with the single ring decay rate, as you see in Fig. 4.10 (b), where we zoom into the marked area from Fig. 4.10 (a). However, approaching this limit, the decay rate oscillates around that value with a shrinking amplitude the larger z becomes. It's surprising that already at rather small values of the inter-ring distance, i.e., at $z/\lambda = 1.3$ the single ring decay rate is reached. The oscillation can be traced back to interference effects that have already been observed in the case of an infinite chain (cf. [9]), for instance. Concluding, in the limit $z \to \infty$ the two rings don't take notice of each other anymore and behave as single rings.
The same result can be observed when studying the most superradiant mode depending on the distance between the rings z/λ, which is plotted for tangential and transverse polarization in Fig. 4.11. For distances $z/\lambda < d/\lambda$ symmetric bright dimers are formed that increase the maximal decay rate. Increasing the distance z, the superradiant decay rate decreases. As before, the curve oscillates while the amplitude of each bump shrinks. With a certain periodicity, it reaches the single ring decay rate already for rather small values of z. For $z/\lambda \to \infty$ the decay rate approaches the single ring decay rate for both polarizations, as anticipated.

Another interesting parameter to vary is the inter-particle distance d/λ as it is plotted in Fig. 4.12 for both, tangential and transverse polarization. In Fig. 4.12 (a), the most subradiant mode is plotted for an increasing distance between the atoms in one ring for both polarizations on an logarithmic scale. Surprisingly, the behaviour is the same in both cases, but the transverse polarization delivers slightly better subradiance. This is also the picture we get from Fig. 4.12 (b),

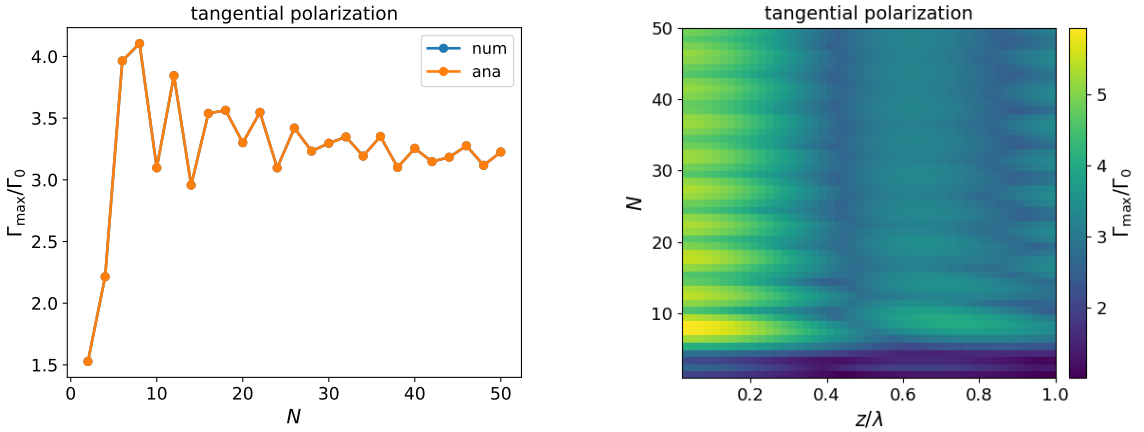

(a) (b)

Figure 4.9: *Most superradiant decay rate as function of the number of atoms in one ring N and the distance between two rings z/λ for tangential dipole orientation and inter-particle distance $d/\lambda = 1/3$.* **(a)** The inter-ring distance is $z/\lambda = 1/3$ and the results arise from analytical and numerical calculations. **(b)** The maximal decay rate is plotted as a function of the number of atoms N and the distance between the rings z/λ in a contour plot.

in which we plot the superradiant decay rate varying with the inter-particle distance d/λ. Again, the superradiant decay rate arising from transversely polarized atoms beats the one for tangential polarization. However, the overall behaviour is the same in both cases. For increasing distance between the atoms the superradiant decay rate decreases.

Bringing the previous plots together, we study the behaviour of the most sub- and superradiant modes depending on the inter-ring and the inter-particle distance for tangential polarization. The result is depicted in Fig. 4.13. The most subradiant decay rate shows an interesting behaviour. The best subradiance is, as we expect, reached for small inter-particle and small inter-ring distances. As soon as both parameters are larger you can suppose that the decay rate underlies a periodicity. However, real subradiance is only in regions for $d/\lambda < 1/2$ or $z/\lambda < 1/2$. In case of small inter-ring distances, dimers are formed and the decay rate is low, as anticipated. On the other hand, if you increase the inter-ring distance while keeping the inter-particle distance low, the rings become independent and the decay rate equals the single ring decay rate. If both parameters, z and d are large, radiant regions become dominant. The $m = 4$ mode is responsible for the dark modes that appear in the region $d/\lambda < 0.5$. For higher distances d as well as z, a superposition of the symmetric eigenstates, namely the $m = 0$ mode, is dominant. For small values of z and increasing d, the $m = 4$ mode is responsible for the subradiance until $d/\lambda \approx 1$. For higher values of d, the modes mix and you receive more states that are superpositions of the eigenstates. Thus, you cannot determine which mode is accountable for the subradiance. However, for larger values of d and z, the $m = 0$ mode is dominant again. Interestingly, we find dark spots at higher distances, as for example around $d/\lambda = 0.6$ and $d/\lambda = 1.6$. These spots are caused by the $m = 0$ mode as well.
Also the superradiant decay rate in Fig. 4.13 (b) has regions where the decay rate is punctually higher than the surrounding. However, one cannot conclude a specific periodicity. The highest

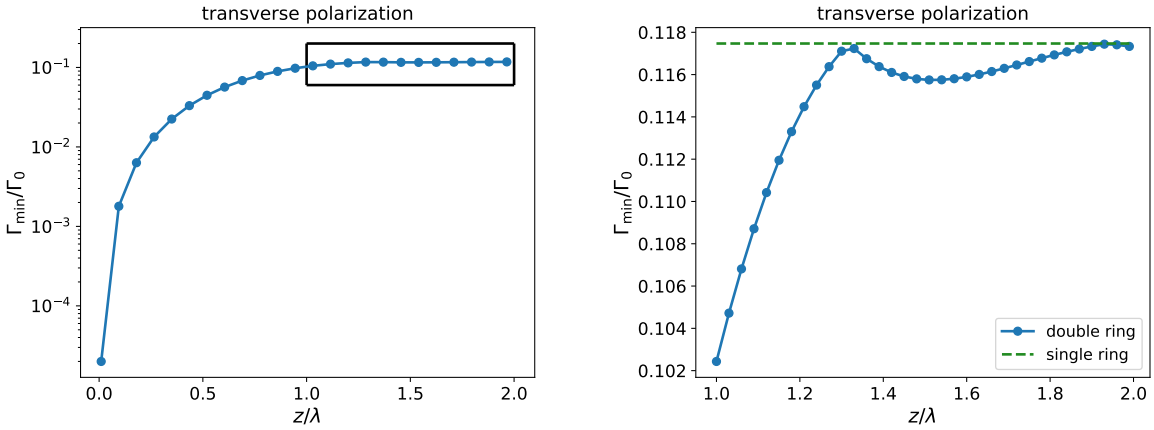

(a) (b)

Figure 4.10: *Most subradiant decay rate* $\Gamma_{\min}$ *depending on the inter-ring distance* z/λ *for inter-particle distances* $d/\lambda = 1/3$ *and* $N = 9$ *atoms for transverse dipole orientation.* **(a)** We plot the most subradiant decay rate for z/λ-values between $z/\lambda = 0$ and $z/\lambda = 2$. We zoom into the region within the black box in **(b)**. Here we include the single ring decay rate for $d/\lambda = 1/3$.

decay rate with more than $\Gamma_{\max}/\Gamma_0 > 11.7$ is obtained for $z/\lambda < 0.25$ and $d/\lambda < 0.1$ as anticipated.

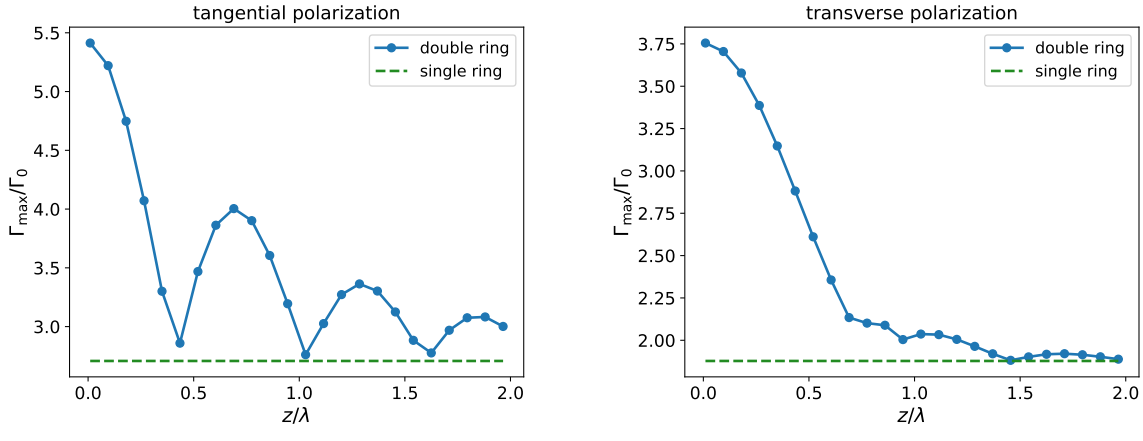

(a) (b)

Figure 4.11: *Superradiant decay rate* $\Gamma_{\max}$ *depending on the inter-ring distance* z/λ *for inter-particle distances* $d/\lambda = 1/3$ *and* $N = 9$ *atoms.* **(a)** The dipole orientation is tangential. **(b)** The dipole orientation is transverse. In both cases we include the single ring decay rate for $d/\lambda = 1/3$ for the corresponding polarization.

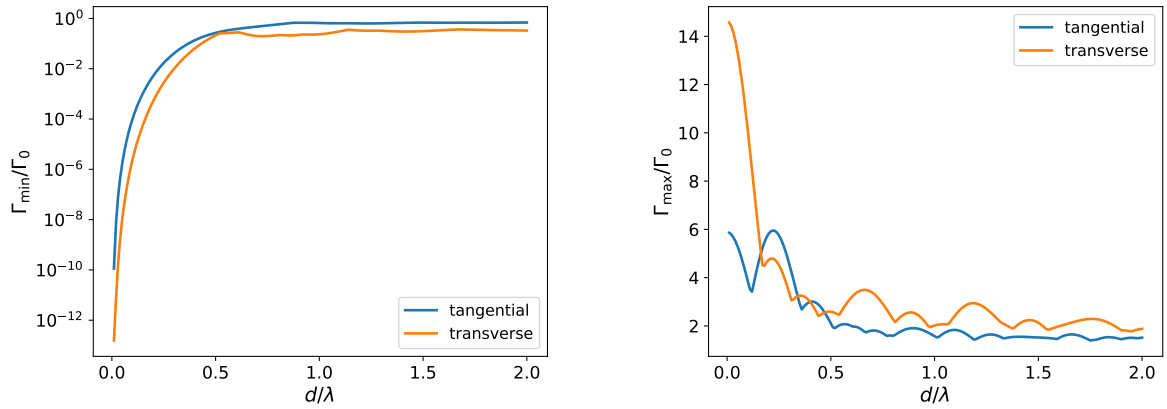

(a) (b)

Figure 4.12: *Most subradiant* **(a)** *and superradiant* **(b)** *decay rate as function of the inter-particle distance d for a ring of $N = 9$ atoms for tangential and transverse polarization.* The inter-ring distance is $z/\lambda = 1/3$.

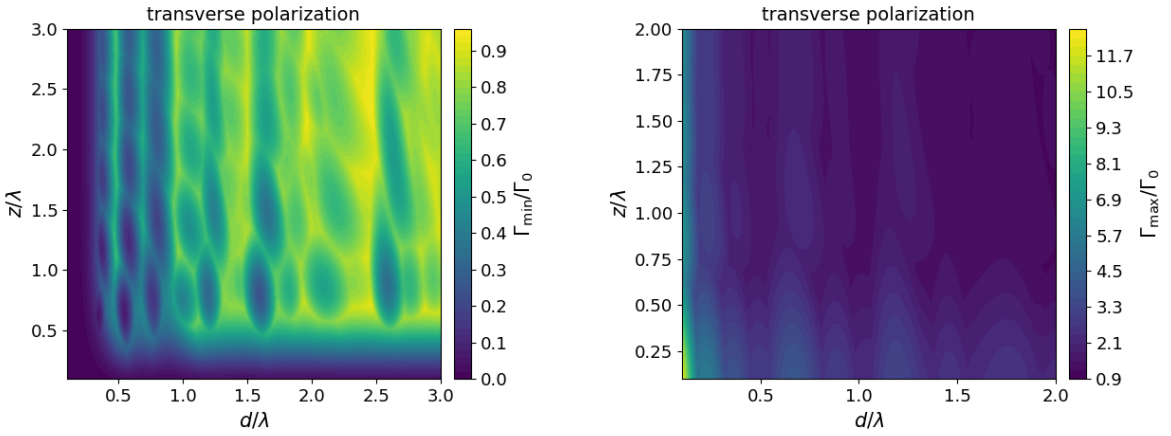

(a) (b)

Figure 4.13: *Most subradiant* **(a)** *and superradiant* **(b)** *decay rate as function of the inter-particle distance d and the inter-ring distance z for $N = 9$ atoms in one ring.* The dipole orientation is transverse.

4.3.4 Radiation field Properties

In order to study the radiation pattern of a double ring, we calculate the field intensity $I(\vec{r}, t) = \langle \vec{E}(\vec{r}, t)\ \vec{E}(\vec{r}, t) \rangle$ as we did in Sec. 3.4 for a single ring.
In case of a double ring we insert the analytical form of the eigenstates given by Eq. (4.8). In the x y-plane, depicted in Fig. 4.14, the pattern of the radiant and superradiant states has a donut-shape. This coincides with the observation in the single ring case. The subradiant modes, as for example the anti-symmetric $m = 4$ mode with a decay rate $\Gamma/\Gamma_0 = 0.07$, show a star-shaped

radiation pattern. Once again this agrees with the pattern of a subradiant mode in the single ring. However, at the anti-symmetric $m = 4$ mode it seems like it's an interstage between donut- and star-shape. This can be led back to the fact that the decay rate is not zero as it would be in the ideal case of subradiance. Here we would obtain a perfect star-shaped pattern. The corresponding radiation pattern in the x z-plane is depicted in Fig. B.2 and Fig. B.3 in Appendix B.

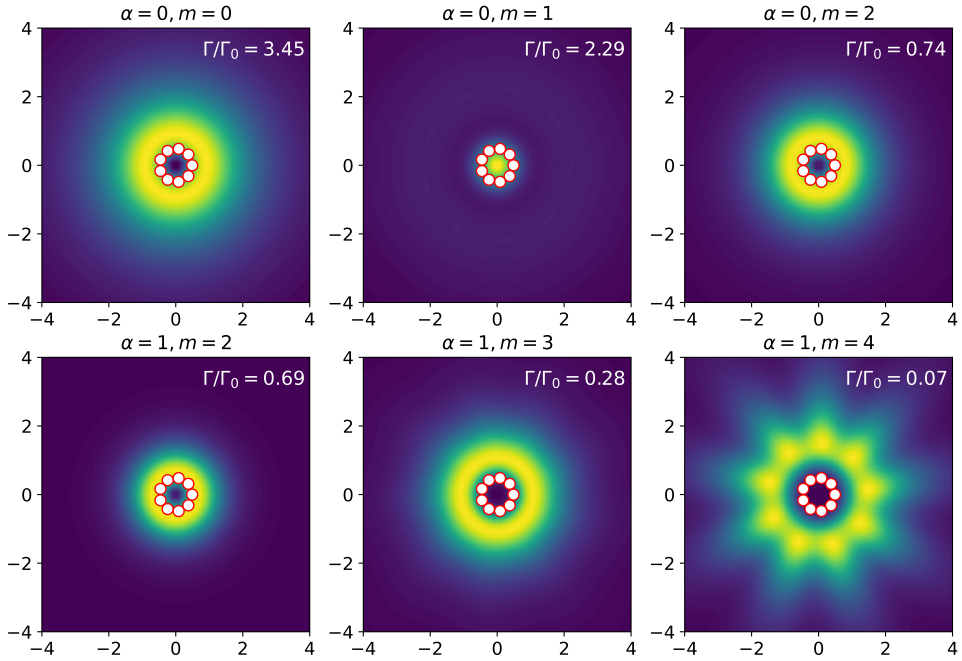

(a)

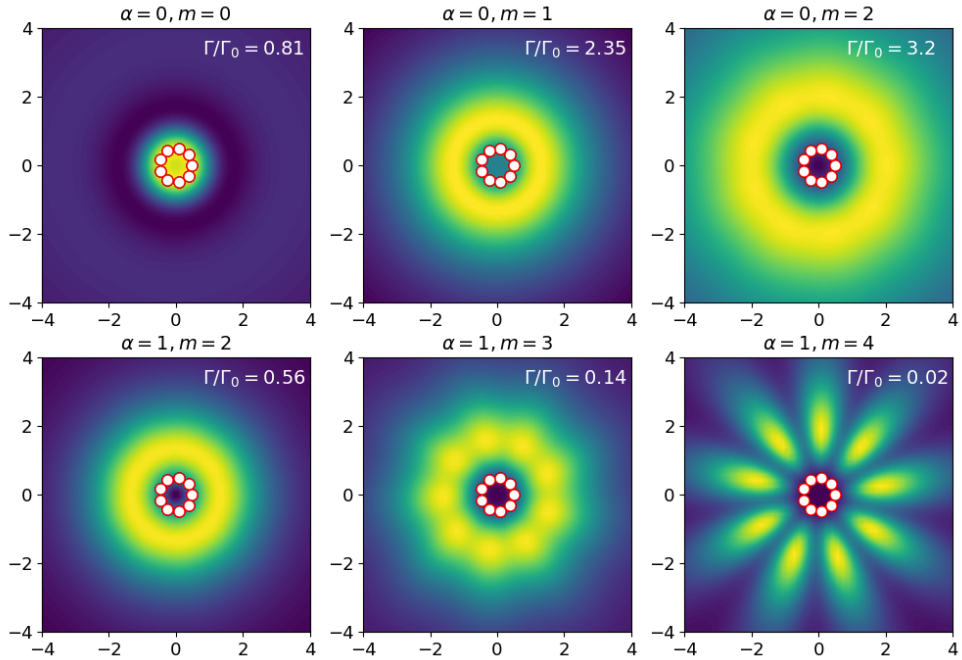

(b)

Figure 4.14: *Radiation pattern of a double ring in the x y-plane.* **(a)** Radiation pattern for tangential polarization. **(b)** Radiation pattern for transverse polarization. The parameters of the system are $d/\lambda = z/\lambda = 1/3$. The observer is located at $d_{\text{obs}}/\lambda = 3R$ above the respective plane.

Chapter 5

Double Ring Structures as they appear in LH-Complexes

The light harvesting apparatus in purple bacteria possesses a multi ring shaped antenna unit that is in charge for absorbing and redirecting light energy to its reaction center. In particular, the light harvesting complex II (LHC-II), depicted in Fig. 5.1, captures photons and transfers the energy over some distance to a LHC-I complex. The larger light harvesting complex I (LHC-I) is then responsible for the subsequent energy-transfer towards the reaction center where it is finally stored as chemical energy. LHC-II is made up of bacterio-chlorophyll (BChl) molecules. In a simplified model of the optically active stucture proposed e.g. by [4], a LH-II is built up of two lower rings of dipoles in the same plane at $z = 0$, which are rotated relative to each other by a certain angle ϕ. These two rings are complemented by a third ring shifted by an additional z component perpendicular to the plane in its position vector. In previous sections we studied systems of two identical coupled rings. However, as shown in Sec. 4.2.2, this simplified model cannot be applied to rings in the same plane which exhibit an additional rotation angle with respect to each other. The aim of the following sections is to generalize the analytical model to an Ansatz that allows us to study the dynamics of the two lower rings.

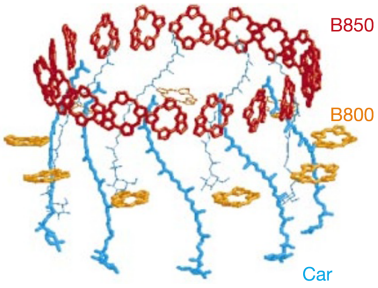

Figure 5.1: *LH-II complex: multi-ring structure as motivation for our studies.* The figure is extracted from [21].

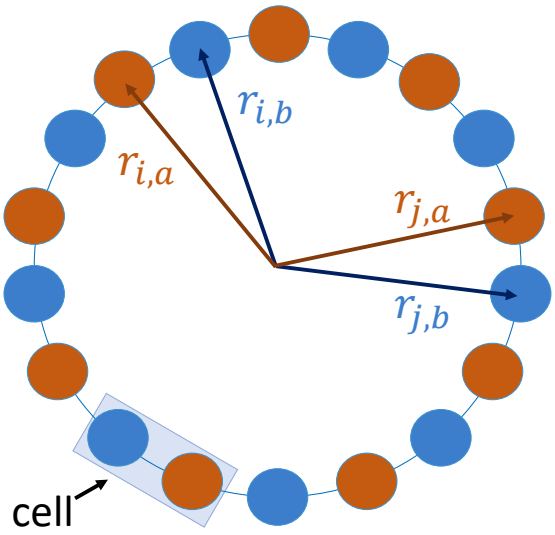

Figure 5.2: *Double ring configuration modeled with two-component cells.*

5.1 Analytical Diagonalization of a Ring with Multi-Component Cells

In order to extend our model to the case of distinct rings, we assume to have one effective symmetric ring made up of N unit cells formed by several atoms, which in general can be of different nature. Here we distinguish between the vector $\vec{R}_j$ that connects the center of the ring with the j-th unit cell with $j = 1, ..., N$ and the vector $\vec{r}_\alpha$ with $\alpha = 1, ..., M$ that connects the center of the cell with the atom component α. This we can add up to a vector $\vec{r}_{j,\alpha} = \vec{R}_j + \vec{r}_\alpha$ that connects the center of the ring with each atom in any cell. Using this notation we can write the effective Hamiltonian as

$$H_{\text{eff}} = \sum_{i,j} \sum_{\alpha,\beta} \hat{\vec{\mu}}_{j,\alpha}\, \mathcal{G}(\vec{r}_{j,\alpha} - \vec{r}_{i,\beta})\, \hat{\vec{\mu}}_{i,\beta}\, \sigma^+_{j,\alpha}\sigma^-_{i,\beta}. \tag{5.1}$$

For a rotationally symmetric ring, it follows that one can apply a rotation operator U of an angle $\Delta\phi = 2\pi/N$ on the dipole operators, the position vectors and the Green's Tensor in the following way

$$\begin{aligned} U\hat{\vec{\mu}}_{j,\alpha} = \hat{\vec{\mu}}_{j+1,\alpha}, \quad U\vec{r}_{j,\alpha} = \vec{r}_{j+1,\alpha}, \\ U\mathcal{G}(\vec{r}_{j,\alpha} - \vec{r}_{i,\beta})U^\dagger \propto U\vec{r}_{j,\alpha} \otimes \vec{r}^{\mathrm{T}}_{j,\alpha}U^\dagger = \vec{r}_{j+1,\alpha} \otimes \vec{r}^{\mathrm{T}}_{j+1,\alpha} \end{aligned} \tag{5.2}$$

and hence with $l = i - j$

$$\begin{aligned} \hat{\vec{\mu}}^\dagger_{j,\alpha}\, \mathcal{G}(\vec{r}_{j,\alpha} - \vec{r}_{i,\beta})\, \hat{\vec{\mu}}_{i,\beta} = \hat{\vec{\mu}}^\dagger_{j,\alpha}\, U^\dagger U\, \mathcal{G}(\vec{r}_{j,\alpha} - \vec{r}_{i,\beta})\, U^\dagger U\, \hat{\vec{\mu}}_{i,\beta} = \\ = \hat{\vec{\mu}}^\dagger_{j+1,\alpha}\, \mathcal{G}(\vec{r}_{j+1,\alpha} - \vec{r}_{i+1,\beta})\, \hat{\vec{\mu}}_{i+1,\beta} \equiv g^l_{\alpha,\beta} \end{aligned} \tag{5.3}$$

as it is only depending on the relative angle $\Delta\phi\ l = \Delta\phi(i - j)$ between the two sites $i - j$. Using this, our Hamiltonian can be written as

$$H_{\text{eff}} = \sum_j \sum_l \sum_{\alpha,\beta} g^l_{\alpha,\beta}\, \sigma^+_{j,\alpha}\sigma^-_{j+l,\beta}. \tag{5.4}$$

Following the same strategy regarding the diagonalization of the Hamiltonian in Sec. 3.2 we use a Spin-wave-Ansatz or a Fourier Transformation, respectively

$$\tilde{\sigma}^{+}_{j,\alpha} = \frac{1}{\sqrt{N}} \sum_{m} \mathrm{e}^{i2\pi mj/N} \sigma^{+}_{j,\alpha}, \quad \tilde{\sigma}^{-}_{j,\alpha} = \frac{1}{\sqrt{N}} \sum_{m} \mathrm{e}^{-i2\pi mj/N} \sigma^{-}_{j,\alpha} \tag{5.5}$$

with the orbital angular momentum $m = 0, \pm 1, \pm 2, \cdots, \lceil \pm (N-1)/2 \rceil$, where $\lceil \cdot \rceil$ is the ceiling function. Inserting this Ansatz into the effective Hamiltonian and using

$$\tilde{g}^{m}_{\alpha,\beta} = \sum_{l} g^{l}_{\alpha,\beta} \mathrm{e}^{i2\pi m' l/N} \tag{5.6}$$

gives

$$\begin{aligned}
H_{\text{eff}} &= \sum_{j} \sum_{l} \sum_{\alpha,\beta} g^{l}_{\alpha,\beta} \ \sigma^{+}_{j,\alpha} \sigma^{-}_{j+l,\beta} = \\
&= \sum_{j} \sum_{l} \sum_{\alpha,\beta} \frac{1}{N} g^{l}_{\alpha,\beta} \sum_{m} \mathrm{e}^{-i2\pi mj/N} \tilde{\sigma}^{+}_{m,\alpha} \sum_{m'} \mathrm{e}^{i2\pi m'(j+l)/N} \tilde{\sigma}^{-}_{m',\beta} = \\
&= \frac{1}{N} \sum_{l} \sum_{\alpha,\beta} g^{l}_{\alpha,\beta} \sum_{m,m'} \mathrm{e}^{i2\pi m' l/N} \sum_{j} \mathrm{e}^{i2\pi (m'-m) j/N} \tilde{\sigma}^{+}_{m,\alpha} \tilde{\sigma}^{-}_{m',\beta} = \\
&= \frac{1}{N} \sum_{\alpha,\beta} \sum_{m,m'} \tilde{g}^{m}_{\alpha,\beta} \sum_{j} \mathrm{e}^{i2\pi (m'-m) j/N} \tilde{\sigma}^{+}_{m,\alpha} \tilde{\sigma}^{-}_{m',\beta} = \\
&= \frac{1}{N} \sum_{\alpha,\beta} \sum_{m,m'} \tilde{g}^{m}_{\alpha,\beta} \delta_{m,m'} N \ \tilde{\sigma}^{+}_{m,\alpha} \tilde{\sigma}^{-}_{m',\beta} = \\
&= \sum_{m} \sum_{\alpha,\beta} \tilde{g}^{m}_{\alpha,\beta} \tilde{\sigma}^{+}_{m,\alpha} \tilde{\sigma}^{-}_{m,\beta}.
\end{aligned} \tag{5.7}$$

In general, the Fourier transformed couplings $\tilde{g}^{m}_{\alpha,\beta}$ for each value of m correspond to a dxd matrix, where d is the number of sites forming the unit cell. In the case considered here, we have only two rings and thus the unit cell consists of two atoms. We obtain the eigenmodes by diagonalizing the corresponding 2x2 $\tilde{g}^{m}_{\alpha,\beta}$ matrix for each value of m. By doing so we arrive at a similar expression for the effective Hamiltonian than we had in previous sections

$$H_{\text{eff}} = \sum_{m} \sum_{\lambda} (J_{m\lambda} - i \frac{\Gamma_{m\lambda}}{2}) \tilde{\sigma}^{+}_{m,\alpha} \tilde{\sigma}^{-}_{m,\beta} \tag{5.8}$$

with $\lambda \in \{0, 1\}$ labelling the two possible solutions of the eigenvalues equation for each value of m. The collective energy-shifts and collective decay rates can be written as

$$J_{m\lambda} = \Re\{\tilde{\omega}^{m}_{\lambda})\} \quad \Gamma_{m\lambda} = -2 \ \Im\{\tilde{\omega}^{m}_{\lambda}\}. \tag{5.9}$$

The eigenvalues are then given by

$$\tilde{\omega}^{m}_{\lambda} = \tilde{g}^{m}_{11} + (-1)^{\lambda} \sqrt{\tilde{g}^{m}_{12} \ \tilde{g}^{m}_{21}}. \tag{5.10}$$

assuming that the dipole orientation of both rings are equal, i.e., $\tilde{g}^{m}_{11} = \tilde{g}^{m}_{22}$. It remains to be checked whether these eigenvalues give rise to the correct decay rates that we receive from numerical calculations.

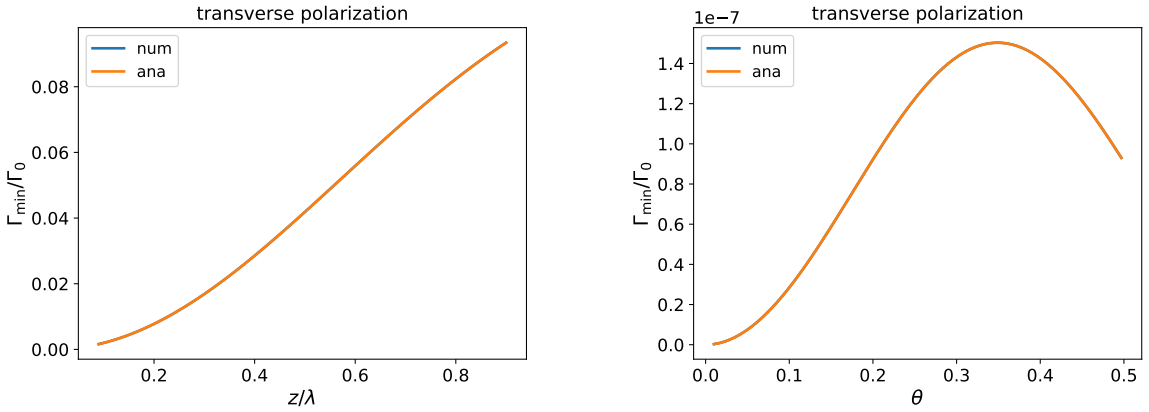

(a) (b)

Figure 5.3: *Smallest subradiant decay rate found by full numerical calculations as well as from our analytical formula as function of the vertical ring distance z and the additional rotation angle $\theta \in [0, 2\pi/9]$* (in radians) *between the rings of $N = 9$ atoms for transverse polarization.* **(a)** The parameters of the system are $d/\lambda = 1/3$ and the phase between the position vectors of the rings is $\theta = 0$. Plotted as a function of the distance z/λ, the numerical results coincide perfectly within the plot resolution with the analytical ones. **(b)** The parameters of the system are $d/\lambda = 1/3$ and $z/\lambda = 0$. Plotted for different angles θ, that we add in the position vectors of one of the rings, the results still coincide. Note the maximum at $\theta \approx 1/3$.

Varying the z-component of the upper ring, the Ansatz from Eq. (4.2) provides the correct eigenvalues as it is discussed in Sec. 4.2. As it is clearly evident in Fig. 5.3 (a), the Ansatz presented in this section delivers the same results and is thus applicable in the case of identical rings (cf. Sec. 4.2.1). However, studying the decay rate for the problem that emerged in Sec. 4.2.2, can be solved with our new Ansatz, as it is obvious in Fig. 5.3 (b). Here the polar angle θ in the position vector of one of the rings is varied. The numerical and analytical results coincide perfectly within the plot resolution.

5.2 Application: Mimicking B850 BChl Double Rings

Above we found an analytical expression to evaluate the eigenstates and eigenenergies of a ring structure consisting of multi-component cells, which allowed us to diagonalize the effective Hamiltonian for any desired rotationally symmetric double ring configuration. As we have shortly stated, LH-II complexes are well studied examples of light harvesting structures of great scientific interest. For that reason we study a geometry mimicking the double ring BChl configuration in LHC-II in more detail.

5.2.1 Geometry of LHC-II

The LHC-II consists of three rings with $N = 9$ bacteriochlorophyll (BChl) molecules extended in the x y-plane as it's visualized in Fig. 5.4. The exact geometric parameters can be extracted from table 5.1. Two of the rings, denoted with α and β, respectively, build a double ring. Both lay in the

Table 5.1: *System parameters.* The radii R_i and the angles θ_i, ν_i, ϕ_i and μ_i of ring i with $i \in \{\alpha, \beta\}$ are presented as they appear in purple bacteria according to [4]. The unit of the dipole moments is debye. The values of parameters corresponding to ring γ aren't listed here as this ring is neglected in the following discussion and we only focus on rings α and β.

R_α / Å	R_β / Å	θ_α / °	θ_β / °	ν_α / °
26.0 ± 0.1	27.5 ± 0.1	96.5 ± 0.7	97.3 ± 0.9	-10.2 ± 0.07
ν_β / °	ϕ_α / °	ϕ_β / °	μ_α / D	μ_β / D
10.2 ± 0.07	-106.6 ± 0.6	60.0 ± 0.9	6.41 ± 0.02	6.30 ± 0.02

same plane at $z/\lambda = 0$ and constitute the B850 nm band. The third ring[1], denoted as γ in Fig. 5.4, is located at $z_\gamma = 16.5 \pm 0.1$ Å above the plane of the double ring in the axial z direction. These BChls pertain to the B800 nm absorption band [4]. The molecules are equally distributed over the rings resulting in an approximate constant angle $\Delta\phi = 2\pi/9$ between 2 BChls (cf. Eq. (3.2)). In Fig. 5.4 spherical coordinates (R_i, ν_i, Z_i) with $i \in \{\alpha, \beta, \gamma\}$ are used in order to define the position vectors of the molecules, whereas spherical coordinates $(\mu_i, \theta_i, \phi_i)$ with $i = \{\alpha, \beta, \gamma\}$ represent their dipole moment vectors. ν_i is the angle that the position vector of an atom in ring i encloses with the x axis and corresponds to the angle ϕ we introduced in Sec. 3. Extracting the corresponding values from table 5.1, the angle between one outer BChl in β and its next nearest neighbour in ring α turns out to be

$$\Delta\nu_{\alpha,\beta} = 20.4^\circ \pm 0.1^\circ. \tag{5.11}$$

The angle ϕ_i in this context is referred to as the polar angle of the transition dipole vector, while θ_i is its azimuthal angle that the dipole vector encloses with the z axis. R_i is the radius of ring i. According to table 5.1, the radii fulfill the relation

$$R_\alpha = (0.945 \pm 0.005)\ R_\beta \tag{5.12}$$

The position vector of the n-th molecule with $n \in [1, 9]$ in the ring i with $i \in \{\alpha, \beta, \gamma\}$ is given by [4]

$$\vec{R}_{i,n} = \begin{bmatrix} R_i\ \cos[2\pi(n-1)/9 + \nu_i] \\ R_i\ \sin[2\pi(n-1)/9 + \nu_i] \\ Z_i \end{bmatrix}, \quad \vec{\mu}_{i,n} = \mu_i \begin{bmatrix} \sin\theta_i\ \cos[2\pi(n-1)/9 + \nu_i + \phi_i] \\ \sin\theta_i\ \sin[2\pi(n-1)/9 + \nu_i + \phi_i] \\ \cos\theta_i \end{bmatrix} \tag{5.13}$$

We assume that the complex BChl molecules can be modeled as two-level atoms as they interact with light in the visible region. The distances derived in [4] and presented in table 5.1 are in the sub-wavelength regime where we expect the dipole-dipole interaction studied in Sec. 2 to be dominant. All previous chapters, where collective phenomena are studied, are based on this assumption. Thus we mimic the BChl double ring, i.e., rings α and β of a LHC-II complex by a double ring.

[1] This ring will be neglected in subsequent discussions as the intra-ring coupling is much stronger than the inter-ring coupling. Thus, one can treat the B850 and B800 band as independent systems.

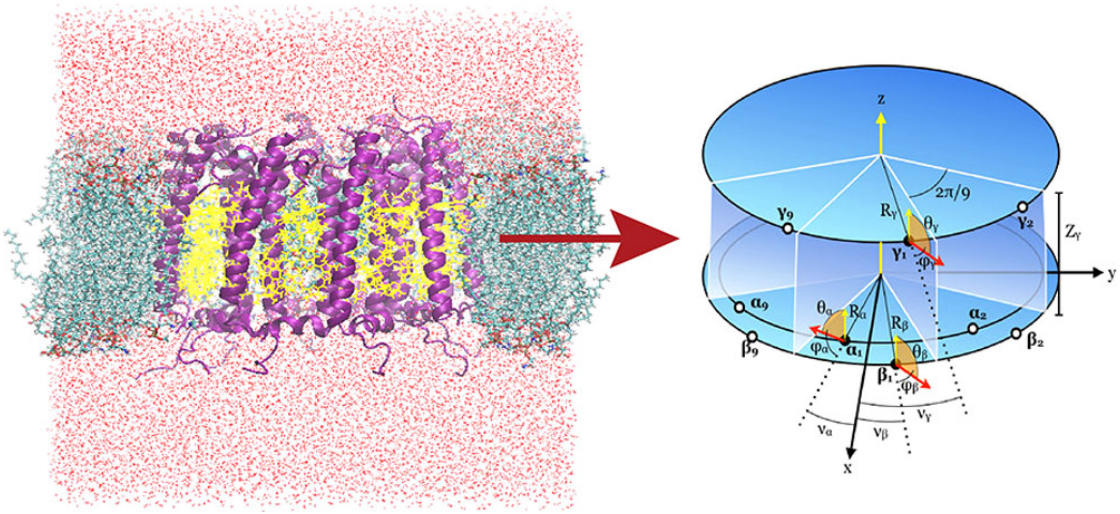

Figure 5.4: *Model of LHC-II.* The figure is extracted from [4].

5.2.2 Collective Decay Rates of the B850 BCHl Molecules modeled by a Double Ring Configuration of Dipole-Coupled Emitters

In order to gain information on important properties of the concrete geometric layout, we have a look at the system in three different variants of geometrical modifications presented and discussed below. In the subsequent discussions we use the ratio given in Eq. (5.12). In our case $R_1 \equiv R_\beta$ and $R_2 \equiv R_\alpha$. In table 5.1, $R_1/\lambda = 0.003$ with $\lambda = 850$ nm which is, in our case, too small for numerical calculations. Instead, we choose in all following calculations $R_1/\lambda = 0.05$, and rescale accordingly the value of R_2. The polar angle in the position vector ν_i of ring i defined in Sec. 5.2.1 corresponds to δ_j with $j = \{1, 2\}$ in our case. The remaining parameters are chosen to be equal.

Case 1: Two rings in the same plane with tangentially aligned dipoles

In this configuration, both rings lay in the same z-plane at $z/\lambda = 0$ and we rotate the position of the atoms in the inner ring α varying over one unit cell from $\delta_2 = 0$ to $\delta_2 = \frac{2\pi}{9}$. The decay rate of the corresponding most subradiant mode for tangential polarization can be seen in Fig. 5.5 (a). Comparing to the dipole vector defined in Eq. (5.13), we choose $\phi_i = 0$ for $i \in \{\alpha, \beta\}$ and $\theta_i = 0$ for $i \in \{\alpha, \beta\}$. In this figure we observe five minima. As we expect, two minima are at $\delta_2 = 0$ and $\delta_2 = 2\pi/9$ corresponding to the case when dimers are built since the distance d between the atoms is much larger than the distance between two atoms in different rings. Surprisingly, we find another local minimum at $\delta_2 = 2\pi/18 \approx 20°$ which agrees approximately with the relative angle in natural LH-II complexes given in Eq. (5.11). As we use a very simplified model, this is already a good agreement. The origin of this minimum is not yet identified but it could be that there is another interesting, most probable a geometric, feature of double rings apart from the formation of dimers leading to the reduction of the decay rate.

Furthermore, we find also two peaks at $\delta_2 \approx 2.0°$ and at $\delta_2 \approx 38°$, magnified in Fig. 5.5 (b). The amplitude of the peaks is limited by the plot resolution. However we could exclude that these peaks are a numerical artefact as they also appear using our analytical Ansatz from Eq. (5.10). We have further studied the emergence of these peaks in Appendix B, in particular, in Fig. B.1. Here, the peaks can be resolved by varying the ratio of the radii R_2/R_1. The higher the ratio,

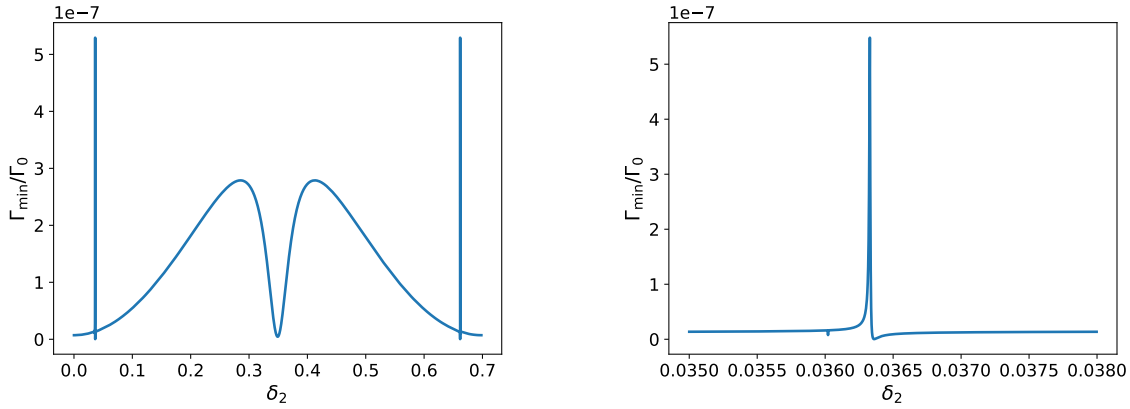

(a) (b)

Figure 5.5: *Most subradiant decay rate depending on an additional phase δ_2 (in radians) in the position vector of the inner ring, for tangentially polarized dipoles and $z/\lambda = 0$.* The radii of the rings are fixed to $R_1/\lambda = 0.05$ and $R_2 = 0.95\ R_1$ as described in case 1. The phase in the position vector of the outer ring is $\delta_1 = 0$. In **(a)** we vary δ_2 from 0 to $2\pi/9 \approx 0.7$. We observe a local minimum of the decay rate at $\delta_2 = 2\pi/18 \approx 0.35$ which approximately coincides with the natural geometry of the LHC-II. There are two peaks at $\delta_2 \approx 2.0°$ which is magnified in **(b)** and $\delta_2 \approx 38°$.

the sharper and higher the peaks are and for smaller ratios the peaks get wider as it's depicted in Fig. B.1 at $R_2/R_1 = 0.8$, for instance. Another observation is that for higher ratios the peak moves to higher values of R_2/R_1. If the inner ring is very small compared to the outer ring, we expect that its rotation is negligible. This expectation is proven to be correct as you approach a constant value of the decay rate in the limit of $R_2/R_1 \to 0$ for different angles δ_2.

The above observations could be interpreted in the following ways. Regarding subradiance[2] the best choice of angles would be at the global minima, i.e. close to where the peaks are, as shown before. However, nature seems to choose the minimum at $\delta_2 \approx 2\pi/18$ [4]. One possible explanation could be that the states at the peaks are really unstable: small vibrations cause a huge change in the decay rate whereas the local minimum in the center is stable and the influence of a positional disorder arising from thermal fluctuations, for instance, is rather small. An explanation for the particular choice of the relative distance $R_2/R_1 = 0.95$ in LH-II complexes based on the information in Fig. B.1 could be, that on the one hand the peaks are far away from the chosen angle $\delta_2 = 2\pi/18$ resulting in an even more stable state and at the same time the decay rate at the center is rather low compared to smaller ratios. Studying the geometric origin (due to the interference of the scattered fields) of the two peaks could be part of future studies.

[2]In natural LH-II complexes, one could think that it is beneficial to have very subradiant and thus long-lived states, but on the other hand it would also be important to collect enough light in order to assure an efficient energy harvesting and transfer. These two factors have to be kept in balance as they go hand in hand. As our model is really simplified, we only focus on achieving the best subradiance.

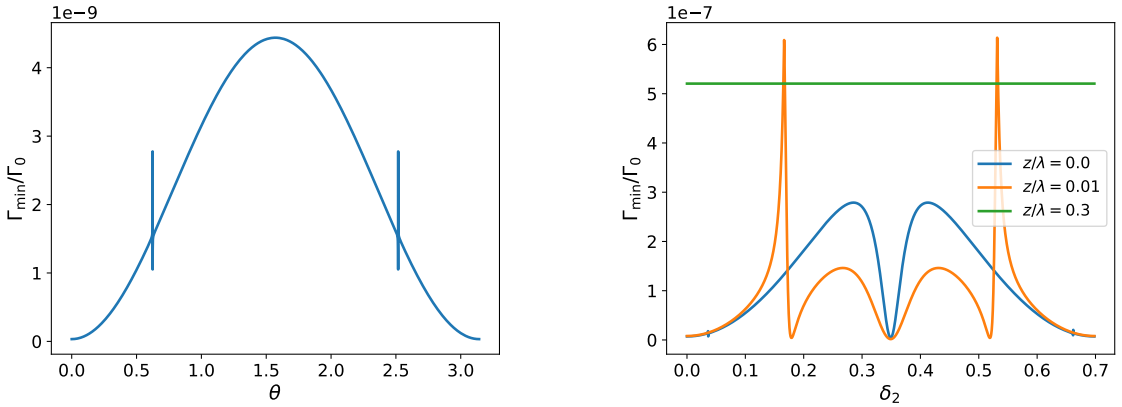

(a) (b)

Figure 5.6: *Further results for case 2 and case 3.* **(a)** Most subradiant decay rate as a function of the azimuthal angle $\theta = \theta_\alpha = \theta_\beta$ (in radians)in the dipole vector $\vec{\mu}$ for $z/\lambda = 0$. **(b)** The subradiant decay rate is plotted as a function of the angle δ_2 (in radians) in the position vector of the atoms in the inner ring for different inter-ring distances z with tangentially polarized dipoles. In both figures the inner ring is rotated around the angle $\delta_2 = 2\pi/18$ and the radii are fixed to $R_1/\lambda = 0.05$ and $R_2 = 0.95\ R_1$, respectively.

Case 2: Two coplanar rings with tangential polarization and an additional vertical component z_{dip} of the dipole orientation.

We define the dipole orientation using spherical coordinates as it is done in Eq. (5.13)

$$\vec{\mu} = |\vec{\mu}| \begin{pmatrix} -R\sin(\phi(j)+\delta)\sin(\theta) \\ R\cos(\phi(j)+\delta)\sin(\theta) \\ R\cos(\theta) \end{pmatrix} \tag{5.14}$$

where R is given in units of λ. We set $|\vec{\mu}| = 1$ and vary the azimuthal angle θ. This way we can have a look at the behaviour of the most subradiant mode starting from transverse polarization ($\theta = 0$) and going to tangential dipole orientation ($\theta = \pi/2$). Here we choose the dipole orientations to be identical in both rings. The most subradiant decay rate has a maximum at $\theta = \pi/2$, i.e., for tangential polarization, and a minima for transverse polarization, as it can be seen in Fig. 5.6 (a). As in case 1, two peaks arise at certain dipole orientations that have a geometric origin. Again, the plot resolution limits their amplitude. In natural LHC-II, the dipole vectors deviate from tangential polarization. In particular, they have a dipole transition vector with an additional polar angle ϕ_i and θ_i for $i \in \{\alpha, \beta\}$ as presented in table 5.1. However, choosing $\phi_\alpha = \phi_\beta = 0$, $\theta_\alpha = 1.68$ and $\theta_\beta = 1.7$, one obtains similar results.

Case 3: Two rings closely above each other for tangential polarization

In this case, we let the atoms position in the second ring get an additional z component. First we choose tangentially polarized atoms and vary the additional polar angle δ_2 in the position vector of the atoms in ring 2 (as already done in case 1), for different values of z. This is shown in Fig. 5.6 (b),

where the blue curve corresponds to the previously studied case of $z = 0$ (Fig. 5.5 (a)), but with a peak resolution that is worse. Increasing the inter-ring distance z results in an equal behaviour as decreasing the radius ratio R_2/R_1. The peaks become wider (cf. orange curve for $z/\lambda = 0.01$), but the most stable minimum remains in the center at $\delta_2 = 2\pi/18 \approx 0.349$. Increasing the inter-ring distance even further results in a constant decay rate. In this case the rings are decoupled and the rotation of one of the ring becomes unimportant.

Next, we vary the dipole orientation from transverse to tangential polarization (cf. Fig. 5.7 (a)) (as it was done in case 2.) The blue curve in Fig. 5.7 (a) corresponds to the curve in Fig. 5.6 (a). For an increasing inter-ring distance z, the minimal decay rate increases. Interestingly, for $z/\lambda = 0.01$ the decay rate has a minimum in the center at $\theta = \pi/2$, i.e., purely tangential polarization. In LHC-II the dipole polarization is basically tangential with small deviations and the rings lay in the same plane at $z/\lambda = 0$ [4]. This corresponds to case 2, where nature would choose the maximal decay rate by fixing tangential dipole polarization. However, in a real system positional disorder occurs that could result in a varying inter-ring distance. Instead of $z/\lambda = 0$, you could effectively have the case of $z/\lambda = 0.01$. Consequently the disorder would cause that fixing the dipole orientation to be tangential corresponds to a minimum in the decay rate (cf. Fig. 5.7 (a)) instead of a maximum (cf. Fig. 5.6 (a)). The curve for $z/\lambda = 0$ has a similar shape as the one for $z/\lambda = 0.1$.

In Fig. 5.7 (b) we plot the minimum discovered in Fig. 5.5 (a) at $\theta = 2\pi/18$ for different inter-ring z and inter-particle d distances. Increasing both, the minimal decay rate Γ_{min} approaches the single atom decay rate Γ_0 as expected. The dark region in Fig. 5.7 (b) for $z/\lambda < 0.3$ and increasing d, could be understood as the formation of dark dimers between the atoms of the same unit cell, despite one ring is rotated around the angle $\delta_2 = 2\pi/18$. However, its origin can be identified if the exact geometric origin of the minimum in Fig. 5.5 (a) is clarified. If you increase the distance between the rings keeping the inter-particle distance low, the subradiant minimum disappears for distances $z/\lambda > 0.8$. Consequently, the minima observed in Fig. 5.5 (a) is subradiant even for higher distances. Such features could be in principle observed using quantum dots, for which inter-particle distances of the order of $d/\lambda = 0.1$ can be realistically achieved with state of the art setups [22].

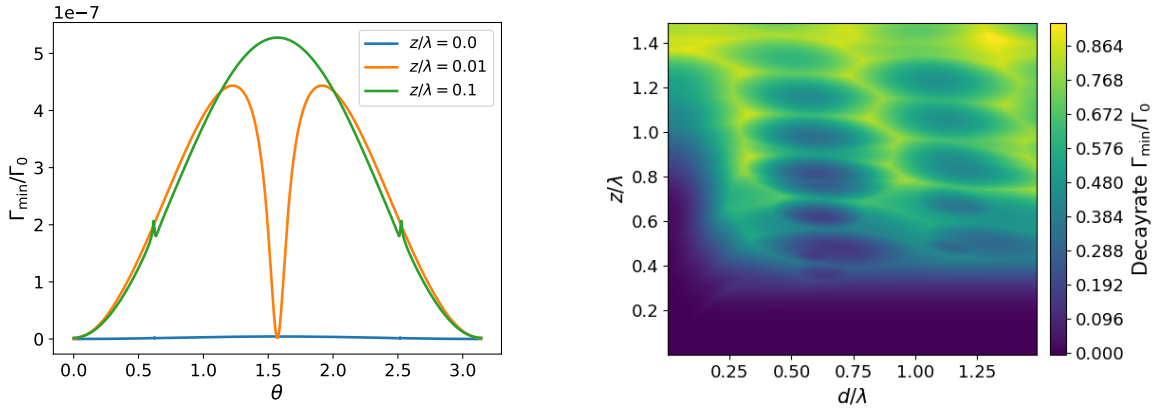

(a) (b)

Figure 5.7: *Results for case 3.* **(a)** The most subradiant decay rate is plotted as a function of the azimuthal angle $\theta = \theta_\alpha = \theta_\beta$ (in radians) of the dipole orientation for different inter-ring distances z. **(b)** Most subradiant decay rate as a function of the inter-ring distance z as well as the inter-particle distance d. In both figures the radii are fixed to $R_2 = 0.95\ R_1$ with $R_1/\lambda = 0.05$ and the inner ring is rotated around an angle $\delta_2 = 2\pi/18$.

Chapter 6

Summary and Conclusions

In this thesis we study the special collective exciton properties of nanoscopic arrays of two-level dipole emitters arranged in a single and double ring configuration. After introducing in Chapter 2 the theoretical framework necessary to describe dipole-dipole interactions and the phenomena of sub- and super-radiance, we start by discussing in Chapter 3 the optical properties of a single ring. As a first starting point we made use of the symmetry of the ring by choosing a Bloch wave solution (that we refer to as spin-wave Ansatz), in order to derive the collective eigenmodes properties, and in particular, the extraordinarily subradiant states arising in this system. In particular, we show that the most subradiant decay rate is exponentially suppressed with the atom number. These results can be directly compared to the dispersion relation and collective decay rates of an infinite chain of quantum emitters. The concept of the light line defined in a chain can be generalized to the ring, if its radius is large enough to neglect the curvature (so that the ring approaches locally to a linear chain). In the finite size case some deviations are expected to arise, but the light line still allows us to identify the conditions required in order to obtain very subradiant states. For a single ring, we also observe that for transverse (tangential) dipole orientations one (two) bright mode(s) occur for very small inter-particle distances, whose decay rates increase linearly with the atom number. Furthermore, we study the relation between the collective decay rates and the energy shifts. The covered energy spectrum increases for an increasing emitter density in a single ring, and the dipole orientation determines whether the bright or the dark modes are higher in energy. Finally, we evaluate the radiation pattern generated by the eigenmode of a single ring. It shows a donut-shape in case of superradiant modes and a star-shaped pattern for subradiant modes.

In Chapter 4 we extend the model of a single ring to describe a structure of two coupled identical rings that preserve the rotational symmetry. In particular, we are interested in the configuration, for which one ring is contained within the x y-plane and the other identical ring is displaced by a vertical distance z. We generalize the previous spin-wave Ansatz and find that for the case of identical rings, the collective eigenmodes can be described as symmetric and anti-symmetric superpositions of the single ring eigenstates with well defined angular momentum, thus leading to a two-band structure for the energy shifts and collective decay rates. The decay rates of the anti-symmetric superposition are always smaller than for a single ring. We show that the decay rate of the most subradiant state for the coupled rings system can exhibit a stronger suppression with the atom number compared to a single ring with the same atom number, for the right choice of system parameters. Instead, the collective decay rates for the symmetric superpo-

sition are always larger than the single ring case and governed by strong oscillations compared to the anti-symmetric ones. One reason could be that the interference effects are stronger because of the higher decay rate. After exploring the parameter space, the overall trend shows that in order to achieve the best sub- and superradiance it is more favourable to arrange N transversely polarized dipoles in a double ring. These results seem to indicate that a double ring structure might be more favourable for the experimental observation of subradiant states using tweezers or quantum dots, as they need a less stringent condition on the inter-particle distances compared to the single ring case (subradiance is already present for $d/\lambda = 1.6$ and $z/\lambda = 0.7$, corresponding to $d = 1.4$ μm and $z = 0.6$ μm for $\lambda = 850$ nm). We also evaluate the field pattern generated by an eigenmode of the double ring structure. As in the single ring case, we find that the a superradiant mode has a donut-shape pattern, whereas for the subradiant modes the radiation field exhibits a star-shaped pattern. For instance, for tangentially polarized atoms and the symmetric superposition of the $m = 0$ mode, the field vanishes at the center of the ring, while for the $m = 1$ mode it is strongly focused at the center. The anti-symmetric superposition provides the opposite behaviour.

Finally, in Chapter 5 we extend our previous spin-wave Ansatz in order to analytically diagonalize the Hamiltonian describing two unequal rings that are coupled but which still preserve rotational symmetry. Having discovered an analytical expression for the eigenvalues, we apply our model to the double ring B850 of the light-harvesting complex II consisting of sub-wavelength spaced BChl molecules commonly appearing in purple bacteria and responsible for harvesting and transferring light to the reaction center. We refer and compare to the results presented in [4]. In our model we assume for simplification that the double ring consists of two-level atoms. Within this model, we attempt to understand nature's particular choice of angles and radii. Rotating one of the double rings contained in the same plane and plotting the most subradiant decay rate as a function of the rotation angle, we observe the emergence of three interesting minima apart from the ones arising from the formation of dimers. However, only the one which is stable against fluctuations coincides approximately with the angle presented in [4] for natural light-harvesting complexes. We justify this choice, keeping our very simplified model in mind, as this minimum is resistant to positional disorder appearing in natural systems.

These discussions and observations provide scope for a large variety of further studies. Not only regarding the special properties of a double ring configuration itself, but in particular regarding the light-harvesting complexes where our model already provides relatively good results. In this context, the next step would be to include as much as possible the real values from [4] in our existing calculations and then extend our model in the next step to a system that takes positional disorder or vibrations into account. Furthermore it would be interesting to figure out the geometric origin of the minima and peaks occurring during rotations of one ring analytically. In future work it would be very interesting to study both, LHC-I and LHC-II, and coming with that, the energy transport between these complexes.

Appendix A

Code-Example

Double Ring Collective Decay Rates Depending on Modes m

In the following a code-example is presented with which one obtains Fig. 4.5. The basics, as system parameters or the effective Hamiltonian, coincide in all other codes we used. We used the Julia programming language including the QoJulia.org quantum optics package [20]. In particular, we used the frameworks QuantumOptics and Collective Spins.

```
using QuantumOptics
using PyPlot;pygui(false);
using CollectiveSpins
using LinearAlgebra

k0=2\pi
#system parameters
N=101
d=1/3
z=1/3

\phi(j) = 2\pi*(j-1)/N  #angle
R = 0.5 * d / sin(0.5 * \phi(2)) #radius of the rings

#position vectors of dipoles
pos=[]
#...in ring 1
vec1(j)=[R*cos(\phi(j)),R*sin(\phi(j)),0.0]
for i=1:N
    pos=push!(pos, vec1(i))
end
#...in ring 2
vec2(j)=[R*cos(\phi(j)),R*sin(\phi(j)),z]
for i=1:N
    pos=push!(pos,vec2(i))
end
```

```
m_list=[0:1:div(N-1,2);] #angular momentum

#dipole transition vectors for transverse orientation
dipor=[0,0,1]
dip=[]
for i=1:N
    dip=push!(dip,dipor)
end
for i=1:N
    dip=push!(dip,dipor)
end

#Coherent coupling and collective decay rate for two coupled dipoles i,j
function CoherentCoupling(ri, rj, \mui, \muj)
    if ri==rj
        return 0.0
    else
        Gre = real(GreenTensor(ri-rj, k0))
        return -3/4*dot(\mui,Gre,\muj)
    end
end

function CollectiveDecay(ri,rj,\mui,\muj)
    if (ri == rj) && (\mui == \muj)
        return 1.0
    elseif (ri == rj) && (\mui != \muj)
        return 0.0
    else
        Gim = imag(GreenTensor(ri-rj, k0))
        return 3/2*dot(\mui,Gim,\muj)
    end
end

#Coherent coupling and collective decay rate for our ring geometry
\Omega(i,j) = CoherentCoupling(pos[i],pos[j],dip[i],dip[j])
\Gamma(i,j) = CollectiveDecay(pos[i],pos[j],dip[i],dip[j])

b = NLevelBasis(2N+1)

#Transition operators
\sigmap=[]
\sigmam=[]

for i=1:2N
    \sigmap = push!(\sigmap,transition(b,i,2N+1))
    #absolute ground to excited state of dipole i
```

```
    \sigmam = push!(\sigmam,transition(b,2N+1,i))
    #excited of dipole i to absolute ground state
end

#effective Hamiltonian
H = sum((\Omega(i,j) - 1im*\Gamma(i,j)/2)*\sigmap[i]*\sigmam[j]
        for i=1:2N, j=1:2N)
#Eigenstates and Eigenvalues
\lambda=eigenstates(dense(H), warning = false)

#List of all decay rates
energyeigenvalues_num(j) = \lambda[1][j]
\Gamma_num(j)=-2*imag(energyeigenvalues_num(j))
dec_num=[]
for k=1:2N+1
    dec_num=push!(dec_num,\Gamma_num(k))
end

eigenst(i)=\lambda[2][i]

\phi(m)= normalize(sum(exp(1im*m*j*2\pi/N)*\sigmap[j] for j=1:N)
                        *nlevelstate(b,2N+1)) #momentum basis
#Overlap of momentum basis with eigenstates

scalar(m,i)= abs.(dagger(\phi(m))*eigenst(i))^2

liste_liste=zeros(length(m_list),2N+1)

for i=1:length(m_list)
    for j=1:2N+1
    liste_liste[i,j]=scalar(m_list[i],j)
    end
end

catcher_sym=[]
catcher_asym=[]

liste_1=liste_liste[1,:]

for i=1:length(m_list)
    m=m_list[i]
    liste_m=liste_liste[m+1,:]
    if m==0
        solutions_sym=[]
        solutions_asym=[]

        for j=1:2
```

```
            index=argmax(liste_m)
            V=eigenst(index)
            liste_m[index]=0.0
            if real(V.data[1])*real(V.data[102]) > 0.0
                catcher_sym=push!(catcher_sym,index)
            end

            if real(V.data[1])*real(V.data[102]) < 0.0
                catcher_asym=push!(catcher_asym,index)
            end

        end

    else

        solutions_sym = []
        solutions_asym = []

        for j=1:4
            index = argmax(liste_m)
            V=eigenst(index)
            liste_m[index]=0.0

            if real(V.data[1]) * real(V.data[102]) > 0.0
                catcher_sym = push!(catcher_sym, index)
            end


            if real(V.data[1]) * real(V.data[102]) < 0.0
                catcher_asym = push!(catcher_asym, index)
            end

        end

    end
end

Gamma_catcher_sym=[]
Gamma_catcher_asym=[]

Gamma_catcher_sym=push!(Gamma_catcher_sym,\Gamma_num(catcher_sym[1]))
Gamma_catcher_asym=push!(Gamma_catcher_asym,\Gamma_num(catcher_asym[1]))

for i=1:(length(m_list)-1)
    Gamma_catcher_sym=push!(Gamma_catcher_sym,
                                \Gamma_num(catcher_sym[2*i+1]))
    Gamma_catcher_asym=push!(Gamma_catcher_asym,
```

```
                                    \Gamma_num(catcher_asym[2*i+1]))
end

plot((2*m_list/N),Gamma_catcher_sym,color="#1f77b4", label="symmetric")
plot(reverse(-2*m_list/N),reverse!(Gamma_catcher_sym),color="#1f77b4")
plot((2*m_list/N),Gamma_catcher_asym,color="#ff7f0e",
                                    label="anti-symmetric")
plot(reverse(-2*m_list/N),reverse!(Gamma_catcher_asym),color="#ff7f0e")

title("transverse polarization")
xlabel(L"\frac{2m}{N}")
ylabel(L"\Gamma_m/\Gamma_0")
legend()
```

Appendix B

Further Ring Properties

Most Subradiant Decay Rate Depending on the Additional Angle δ_2 in the Position Vector of Ring 2

Fig. B.1 provides supplementary information for Sec. 5.2.2. Here we study the curve presented in Fig. 5.5 (a) for different ratios R_2/R_1 in order to resolve the two sharp peaks. We can exclude that these peaks are divergences. Further we see that for higher ratios the peaks become sharper and move outwards, towards $\delta_2 = 0$ and $\delta_2 = 2\pi/9$. For smaller ratios the curve approaches a constant value, as expected.

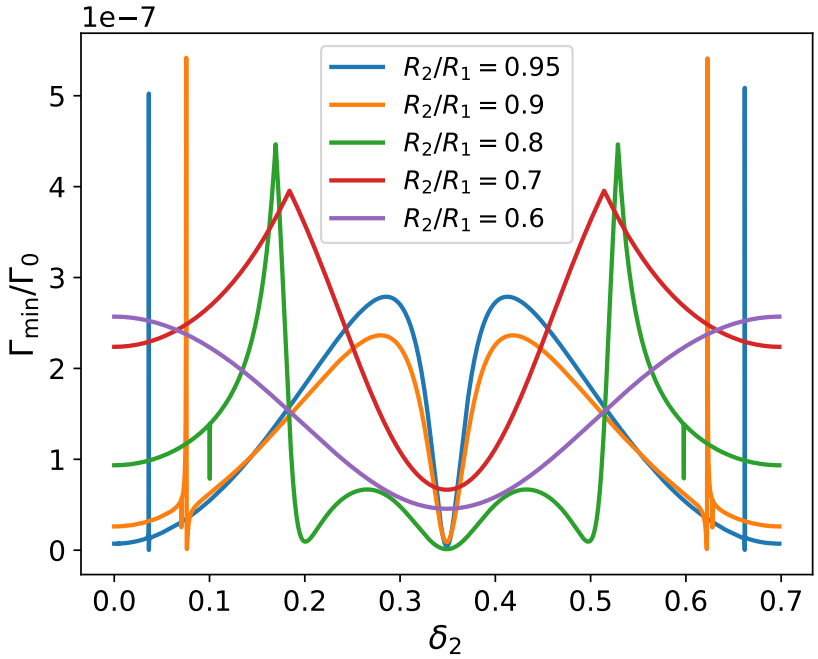

Figure B.1: *Most subradiant decay rate of a double ring configuration for different ratios of radii R_2/R_1 depending on the additional polar angle δ_2 in the position vector of ring 2.* The rings are in the same plane with $z/\lambda = 0$. The dipoles are tangentially polarized.

Radiation Pattern of a Double Ring in the x z-Plane

We present the resulting radiation pattern of a double ring configuration at different modes for tangential and transverse dipole orientation in the x z-plane in Fig. B.2 and Fig. B.3.

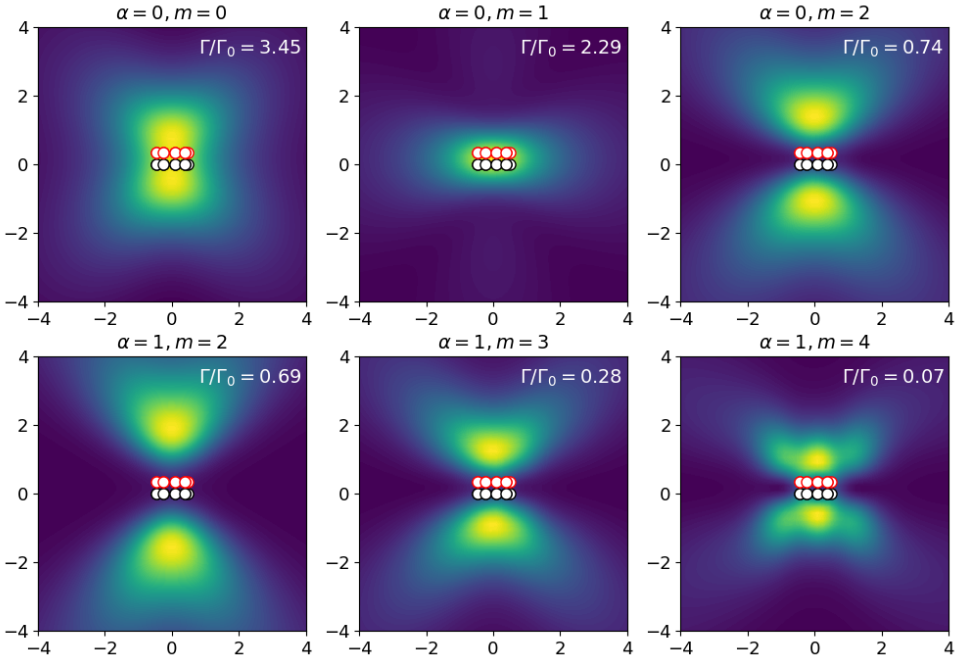

Figure B.2: *Radiation pattern of a double ring in the x z-plane for tangential polarization.* The parameters of the system are $d/\lambda = z/\lambda = 1/3$. The observer is located at $d_{\mathrm{obs}}/\lambda = 3R$ above the respective plane.

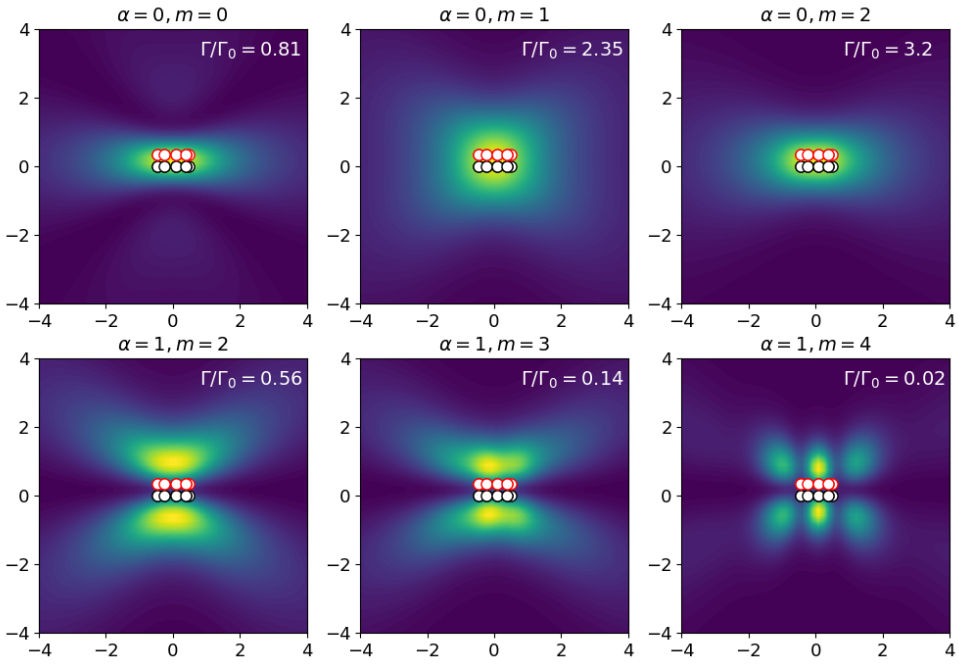

Figure B.3: *Radiation pattern of a double ring in the x z-plane for transverse polarization.* The parameters of the system are $d/\lambda = z/\lambda = 1/3$. The observer is located at $d_{\text{obs}}/\lambda = 3R$ above the respective plane.

Bibliography

[1] Blankenship, "Comparing photosynthetic and photovoltaic efficiencies and recognizing the potential for improvement," *Science (New York, N.Y.)*, vol. 332, pp. 805–9, 05 2011.

[2] W. E. Council, "Renewable energy projects handbook," pp. 12–15, 2004.

[3] W. Jianlan, . M. A. C. M. . Department of Chemistry, Massachusetts Institute of Technology, L. Fan, R. J. Silbey, C. Jianshu, and M. Jian, "Efficient energy transfer in light-harvesting systems: Quantum-classical comparison, flux network, and robustness analysis," *Journal of Chemical Physics*, vol. 137, 11 2012.

[4] D. Montemayor, E. Rivera, and S. Jang, "Computational modeling of exciton-bath hamiltonians for lh2 and lh3 complexes of purple photosynthetic bacteria at room temperature," *The Journal of Physical Chemistry B*, vol. 122, 03 2018.

[5] G. Scholes and G. Fleming, "On the mechanism of light harvesting in photosynthetic purple bacteria: B800 to b850 energy transfer," *The Journal of Physical Chemistry B*, vol. 104, 03 2000.

[6] M. Moreno-Cardoner, D. Plankensteiner, L. Ostermann, D. Chang, and H. Ritsch, "Extraordinary subradiance with lossless excitation transfer in dipole-coupled nano-rings of quantum emitters," 01 2019.

[7] R. H. Dicke, "Coherence in spontaneous radiation processes," *Phys. Rev.*, vol. 93, pp. 99–110, Jan 1954.

[8] S. J. Masson and A. Asenjo-Garcia, "Atomic-waveguide quantum electrodynamics," *Phys. Rev. Research*, vol. 2, p. 043213, Nov 2020.

[9] A. Asenjo-Garcia, M. Moreno-Cardoner, A. Albrecht, H. J. Kimble, and D. E. Chang, "Exponential improvement in photon storage fidelities using subradiance and "selective radiance" in atomic arrays," *Phys. Rev. X*, vol. 7, p. 031024, Aug 2017.

[10] S. Maier, M. Brongersma, P. Kik, and H. Atwater, "Observation of near-field coupling in metal nanoparticle chains using far-field polarization spectroscopy," *Physical Review B*, vol. 65, 05 2002.

[11] J. Cremer, *Dipole-Coupled Nano-Ring(s) of Quantum Emitters*. University of Innsbruck, Oct 2019.

[12] J. Herek, W. Wohlleben, R. Cogdell, D. Zeidler, and M. Motzkus, "Quantum control of energy flow in light harvesting," *Nature*, vol. 417, pp. 533–5, 06 2002.

[13] "Quantum biology of the PSU." `https://www.ks.uiuc.edu/Research/psu/psu.html`, 2006.

[14] C. I. Branden and J. Tooze, *Introduction to protein structure*. New York: Garland Science, 1998.

[15] D. Plankensteiner, *Collective dynamics and spectroscopy of coupled quantum emitters*. University of Innsbruck, May 2019.

[16] R. Loudon, *The Quantum Theory of Light*. Oxford University Press, 2000.

[17] R. H. Lehmberg, "Radiation from an n-atom system. i. general formalism," *Phys. Rev. A*, vol. 2, pp. 883–888, Sep 1970.

[18] L. Ostermann, *Collective Radiation of Coupled Atomic Dipoles and the Precise Measurement of Time*. University of Innsbruck, June 2016.

[19] Masson, J. Stuart, and A. Asenjo-Garcia, "Atomic-waveguide quantum electrodynamics," *Phys. Rev. Research*, vol. 2, p. 043213, Nov 2020.

[20] S. Krämer, D. Plankensteiner, L. Ostermann, and H. Ritsch, "Quantumoptics.jl: A julia framework for simulating open quantum systems," *Comput. Phys. Commun.*, vol. 227, pp. 109–116, 2018.

[21] J. Herek, W. Wohlleben, R. Cogdell, *et al.*, "Quantum control of energy flow in light harvesting," *Nature*, vol. 417, Jan 2002.

[22] J. Vukajlovic-Plestina, W. Kim, V. Dubrovski, G. Tütüncüoğlu, M. Lagier, H. Potts, M. Friedl, and A. Fontcuberta I Morral, "Engineering the size distributions of ordered gaas nanowires on silicon," *Nano Letters*, vol. 17, pp. 4101–4108, July 2017.

Eidesstattliche Erklärung

Ich erkläre hiermit an Eides statt durch meine eigenhändige Unterschrift, dass ich die vorliegende Arbeit selbständig verfasst und keine anderen als die angegebenen Quellen und Hilfsmittel verwendet habe. Alle Stellen, die wörtlich oder inhaltlich den angegebenen Quellen entnommen wurden, sind als solche kenntlich gemacht.

Die vorliegende Arbeit wurde bisher in gleicher oder ähnlicher Form noch nicht als Magister-/Master-/Diplomarbeit/Dissertation eingereicht.

Innsbruck, den 22.02.2022